nature geoscience

Article

https://doi.org/10.1038/s41561-025-01671-x

Seismic full-waveform tomography of active cratonic thinning beneath North America consistent with slab-induced dripping

Received: 8 September 2023

Accepted: 17 February 2025

Published online: 28 March 2025

Check for updates

Junlin Hua [1,2,3,4], Stephen P. Grand[3], Thorsten W. Becker [3,4,5], Helen A. Janiszewski[6], Chujie Liu[3], Daniel T. Trugman[7] & Hejun Zhu[8]

Continental cratons are characterized by thick lithospheric roots that remain intact for billions of years. However, some cratonic roots appear to have been thinned or completely removed in the geological past. The mechanisms for thinning have been difficult to distinguish for these past events. Here we present a full-waveform seismic tomographic model for North America that allows the resolution of fine-scale structures and reveals an extensive craton-thinning event that is ongoing. The seismic images show extensive drip-like features that suggest the transport of lithospheric materials from the base of the craton beneath the central United States to the mantle transition zone, and thus active lithospheric thinning. Geodynamic modelling suggests that the dripping may be mobilized by large-scale mantle flow induced by the sinking of the Farallon slab that is currently in the lower mantle. Dripping lithosphere could be further facilitated by prior lithospheric weakening, for example by volatiles released from the slab. Our seismological observations of active extensive thinning of cratonic lithosphere support lithospheric removal could be a result of external mantle processes, which we hypothesize may include the deep mantle effects of subduction.

Cratons are old (no younger than Proterozoic) regions that make up ~60% of continental lithosphere[1] and are often underlain by thick lithosphere that can extend to a depth of over 200 km (refs. 1,2). Cratons are believed to have been stable overall over billions of years due to their near neutral effective buoyancy and high viscosity[3,4]. However, the North China Craton lost its root during the Mesozoic[5], indicating that the stability of cratons is not universal. Different mechanisms have been proposed for the loss of cratonic lithosphere, including convective removal[6], flat-slab rollback[7] and erosion with melting[8,9]. Other studies suggest that the cratonic lithosphere is not stable through history but subject to reworking[10]. Given that these examples are from processes in the geological past, it is not straightforward to distinguish between different mechanisms, and observations of an ongoing craton-thinning event would offer a unique perspective to the puzzle.

North America is an ideal place to study the present-day behaviour of cratons. Core continental North America consists of multiple

[1]Laboratory of Seismology and Physics of Earth's Interior, School of Earth and Space Sciences, University of Science and Technology of China, Hefei, China. [2]State Key Laboratory of Precision Geodesy, University of Science and Technology of China, Hefei, China. [3]Department of Earth and Planetary Sciences, Jackson School of Geosciences, The University of Texas at Austin, Austin, TX, USA. [4]Institute for Geophysics, Jackson School of Geosciences, The University of Texas at Austin, Austin, TX, USA. [5]Oden Institute for Computational Engineering and Sciences, The University of Texas at Austin, Austin, TX, USA. [6]Department of Earth Sciences, University of Hawai'i at Mānoa, Honolulu, HI, USA. [7]Nevada Seismological Laboratory, University of Nevada, Reno, Reno, NV, USA. [8]Department of Earth and Space Sciences, Southern University of Science and Technology, Shenzhen, China.
e-mail: junlin_hua@ustc.edu.cn

https://doi.org/10.1038/s41561-025-01671-x

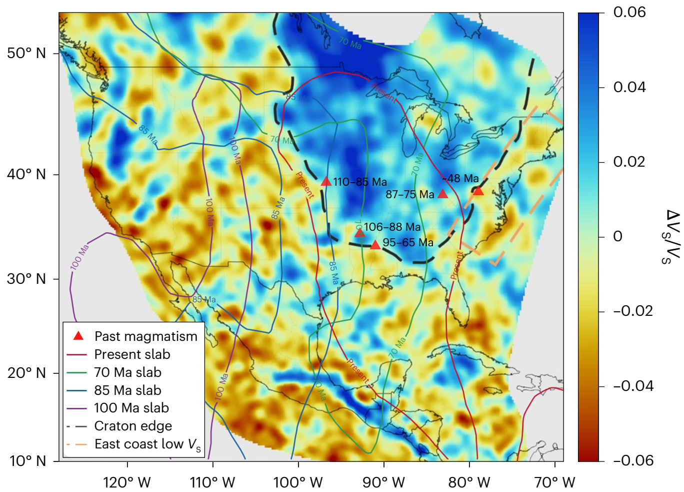

Fig. 1 | Isotropic V_S distribution at a depth of 200 km, revealing the craton root. The background colour shows the V_S perturbation. The craton root is characterized by a high V_S and is outlined by a black dashed line. Low-V_S anomalies along the east coast are outlined by a light brown dashed line. Red triangles show past magmatism around the craton, with their ages labelled. Solid lines with different colours show surface projections of current and past locations of the Farallon slab at a depth of 800 km with respect to the North American plate[32].

Archaean cratons and volcanic arcs accreted during the Proterozoic. Although most cratonic regions in the United States were stabilized during the Proterozoic from 1.8 to 1.35 billion years ago (Ga)[11], they still share key features with their Archaean counterparts, including very thick lithosphere[2] and surrounding kimberlite volcanism[12]. Meanwhile, thanks to dense seismometer deployments, the central and eastern United States cratons can be studied in detail seismically.

In this Article we present a full-waveform tomography model for North America (Fig. 1), named Seismic Adjoint Tomography of North America (SATONA). Compared with existing tomographic models of North America, SATONA focuses more on fitting the detailed shape of waveforms at relatively high frequencies to better reveal fine-scale structures. SATONA reveals clear lithosphere–asthenosphere boundaries (LABs) for the craton, and high-seismic-velocity materials beneath the craton from the LABs to the mantle transition zone (MTZ). These high-velocity, drip-shape features indicate thermo–chemical differences relative to the surrounding mantle that probably originate from the cratonic lithosphere. To find the cause for such dripping, we test the influence of the lower mantle Farallon slab on upper-mantle convective flow through geodynamic modelling, and find that the dripping may be a consequence of slab sinking, aided by other processes. These findings lead us to propose a potential mechanism for craton thinning—large-scale downwelling induced by a deep-seated slab that mobilizes the craton, possibly mediated by fluid release, leading to partial removal of the cratonic lithosphere.

Dripping cratonic lithosphere

The SATONA model is obtained through full-waveform adjoint tomography. During inversion, we maximize the correlation coefficient between synthetic and observed waveforms[13]. Hence, besides the arrival times of the seismic phases, the detailed shapes of the phases, including secondary arrivals, are required to match the data. In this study, both synthetic seismograms and adjoint kernels were calculated with SpecFem3D Globe[14,15], and all available stations in the study region were utilized (Extended Data Fig. 1). We used multiple body and surface wave phases to constrain S- and P-wave velocities[16]. To optimize computational efficiency and avoid local minima, the inversion consists of two stages[17]: a coarse-grid stage using 206 earthquakes and a fine-grid stage using 110 earthquakes with higher quality (Extended Data Fig. 1). We incorporate a mini-batch algorithm[18,19] by using a subset of earthquakes in each iteration, which, compared with the common full-waveform tomography practice of using only a few tens of iterations on supercomputers[16], enables a total of 216 iterations with four graphics processing units (GPUs).

With these, the improvement on the correlation coefficient and the arrival time difference between synthetic and observed waveforms is substantial (Extended Data Fig. 2). Body waves show higher accuracy in timing than surface waves, whereas surface waves have the correlation better recovered. Nonetheless, the vast majority of both wave types show correlation coefficients over 0.9, suggesting an excellent fitting of the waveform shape.

Detailed mantle structures are imaged in SATONA. S-wave velocity (V_S; Extended Data Fig. 3) at a depth of 100 km correlates well with tectonic regions[20], and at greater depths, the model captures features such as the Cascadia slab in fine detail. P-wave velocity (V_P; Extended Data Fig. 4), which is independently inverted for, shows similar patterns. A resolution test with only 16 iterations (versus 206 for the full model) shows that V_S has good resolution down to 1,000 km, especially within the upper mantle (Extended Data Fig. 5). V_P also has good resolution down to the MTZ, but deeper resolution is reduced (Extended Data Fig. 5). We only discuss regions with reliable resolution. The velocity perturbation model also shows some horizontally aligned anomalies near reference model discontinuities (for example, near a depth of 660 km in Fig. 2a,b). However, as discontinuity depths are taken from previous models upon initialization of the inversion, these anomalies might be introduced to reconcile inaccuracies about discontinuity depth in those starting models to make the absolute velocity accurate, and are therefore not interpreted much in this study.

The cratonic lithosphere is well-imaged in the model. At a depth of 200 km, a broad region beneath the central and eastern United States shows high V_S (Fig. 1), marking the geographic extent of the deep cratonic root. Cratonic LABs are clearly characterized as a velocity decrease with depth around 200 km in both V_S and V_P (Fig. 2a,b and Extended Data Fig. 6).

Beneath the cratonic LAB, extensive high-V_S anomalies are observed down to the MTZ (Fig. 2 and Extended Data Fig. 3). A specific model resolution test (Extended Data Fig. 7) suggests that these anomalies can be well-imaged with our dataset and inversion strategy. Similar high-velocity anomalies are also found in previous models[21–25] (Extended Data Fig. 8). However, without the help of multiple seismic phases, their cratonic lithosphere is not well constrained (Extended Data Fig. 8), and the deep structures sometimes extend into the lithosphere depth range, making them harder to interpret.

To distinguish whether these high-V_S anomalies originate from the cratonic lithosphere, we convert V_S and V_P perturbations of the dripping bodies to temperature and compositional perturbations. Compared with V_S, V_P shows much weaker anomalies at 300–500-km depths (Extended Data Fig. 6), distinct from the strong V_P anomaly in the Cascadia slab, suggesting a potentially different composition. To constrain the compositional perturbation, two endmembers are considered. One composition is assumed to be pyrolite[26] and the other to be cratonic lithosphere. We estimate a representative major element composition for the craton from kimberlite xenoliths (Extended Data Fig. 9). The V_S and V_P for these two endmember compositions at different temperatures and pressures are then calculated using Perple_X[27,28], accounting for anelastic effects[29]. Derivatives of V_S and V_P with respect to temperature and composition are obtained, and velocity anomalies are then converted to temperature and compositional perturbations. We performed the conversion for all geographic locations based on a smoothed version of SATONA (Extended Data Fig. 9) to eliminate bias due to the misalignment of V_S and V_P anomalies.

Taking the compositional perturbation between the endmembers as unity, at all depths, the high-V_S anomalies show 20–50% more cratonic composition than the ambient mantle (Extended Data Fig. 9),

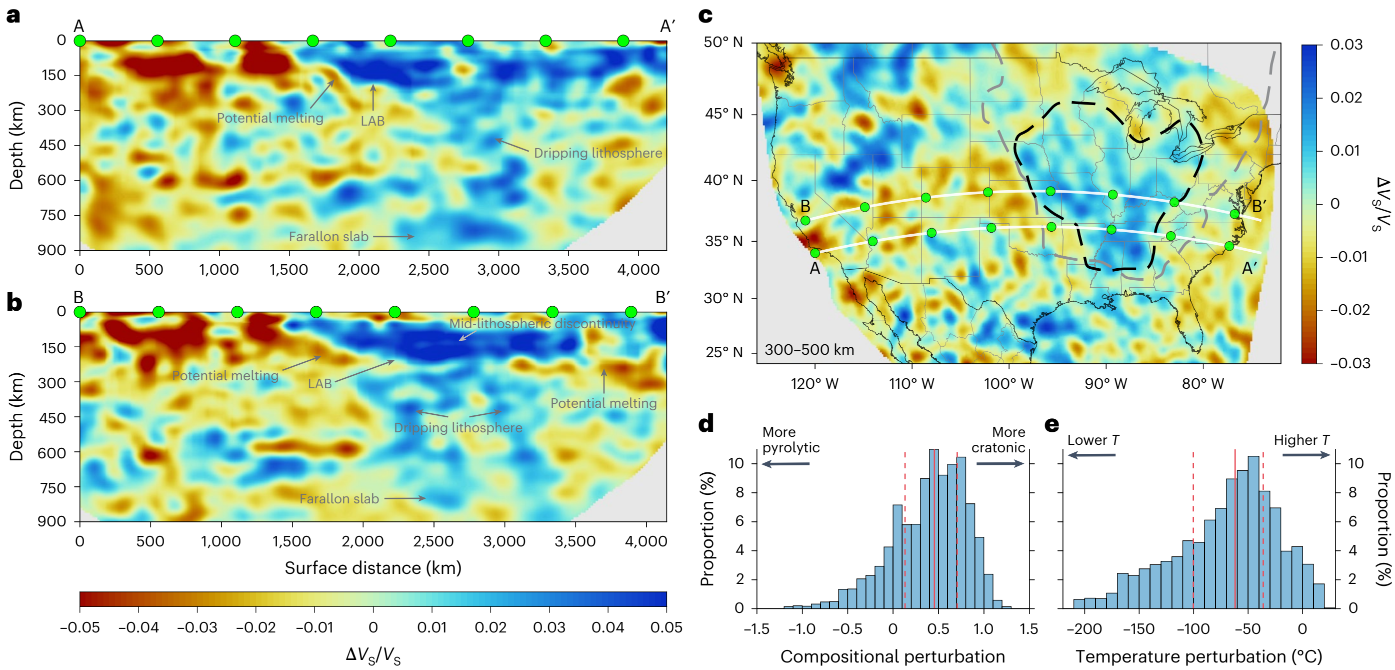

Fig. 2 | The dripping cratonic lithosphere. a,**b**, V_S perturbation profiles across high-velocity dripping anomalies at different latitudes (AA′ for **a** and BB′ for **b**). Locations of these profiles are shown in **c**. Green dots at the top are geographic markers. Important features in the cross-sections are labelled. **c**, Map of the average V_S perturbation between depths of 300 and 500 km. The grey dashed line outlines the craton root as in Fig. 1, and the black dashed line outlines where the dripping high-V_S body is evident at this depth range. White lines show the locations for the profiles in **a** and **b**, and green geographic markers correspond to those at the top of the cross-sections. **d**, Histogram of the converted compositional perturbation distribution of dripping bodies (within the black dashed line in **c**) at a depth of 350 km. Each sample represents one geographic location. Zero in this plot represents the average composition for all regions with good resolution, and positive or negative values mean more cratonic or more pyrolytic, respectively. The red solid line shows the median value, and the dashed lines show 25% and 75% percentiles. **e**, As in **d**, but for the temperature perturbation.

which indicates the entrainment of lithospheric material. Especially below 300 km, due to the phase transition of orthopyroxene at ~320 km (ref. 28), the dependence of the V_S–V_P discrepancy on composition becomes stronger, making the compositional perturbation better constrained. At a depth of 350 km, the median of the dripping high-V_S bodies has 45% more cratonic composition than normal (Fig. 2d), which is close to the 75% percentile of compositional perturbations for regions excluding the dripping area (Extended Data Fig. 9m), indicating that the high-V_S anomalies are substantially more cratonic than normal. Despite having higher V_S, when converted to temperature perturbation, we found that these anomalies are only ~60 °C colder than normal (Fig. 2e). Even for less constrained depths, the thermal anomaly is less than 200 °C (Extended Data Fig. 9j). This test demonstrates that these compositionally distinct anomalies with slightly lower temperatures could be drips from the deep part of the lithosphere, and they are hereafter referred to as dripping anomalies.

Deep-seated slab-induced dripping

Similarly imaged dripping anomalies in the region have previously been interpreted as remnant slabs[22] or dripping due to Rayleigh–Taylor instability[30], but both mechanisms have some limitations. For slab relics, the relative values of V_S and V_P anomalies do not match those of the Cascadia slab, whose V_P anomalies are much stronger (Fig. 2c and Extended Data Fig. 6). There is also no evidence of arc volcanism in the study region since at least the Mesozoic[31], which is a long time for stalling thermal anomalies to homogenize with the surroundings. In particular, large-scale downward flow probably occurred in this region for 70 Myr (ref. 32), so it is not likely for slab relics to persist. If the anomalies are purely from a Rayleigh–Taylor instability due to a dense craton root[30], it is hard to explain the relatively weak V_P anomaly for the drips (Extended Data Fig. 6), because, with the inclusion of a large percentage of dense minerals such as garnet, V_P would also be increased[33]. Meanwhile, if a uniform dense root is common among cratons, similar dripping would probably be observed beneath every craton, and probably have occurred for over a billion years and hence might have consumed all dense material.

We propose a potential mechanism whereby the deep Farallon slab is the main driver of dripping, although it is in the lower mantle and not connected to the surface at present. To evaluate the dynamic influence of the Farallon slab, we calculated mantle flow[34] for two different density structures (Fig. 3): mantle with or without the Farallon slab. These structures are modified from a global mantle tomography model[35]. The results show that large-scale mantle flow is strongly controlled by the Farallon slab, which pulls shallow mantle from the east, west and north to the dripping area, where these mantle materials flow downward (Fig. 3a), in line with previous work[36]. Such flow is only predicted when the Farallon slab is present (Fig. 3a,b), and is absent without it (Fig. 3c,d). The Farallon slab may induce horizontal mantle flow over a domain wider than ~3,000 km from the sinker (Fig. 3a versus 3c), and associated shear flow may serve to thin and entrain the base of the craton (Fig. 3b). In other words, even though the imaged dripping area has a relatively limited extent as in Fig. 2c, the material involved in the sinker may come from a wider region. Such basal erosion by slab-induced flow leading to dripping removal of continental lithosphere may be assisted by prior weakening of the lithosphere, for example, due to volatile influx from the slab. Associated slab-induced dripping could have started at ~70 Ma, as the Farallon slab has stayed at a similar relative location with respect to North America since then[32] (Fig. 1), and the rate of thinning might have been greater when the slab was shallower in the past.

Based on the tomographic model, by assuming the V_S anomaly is proportional to the amount of cratonic material, given assumptions

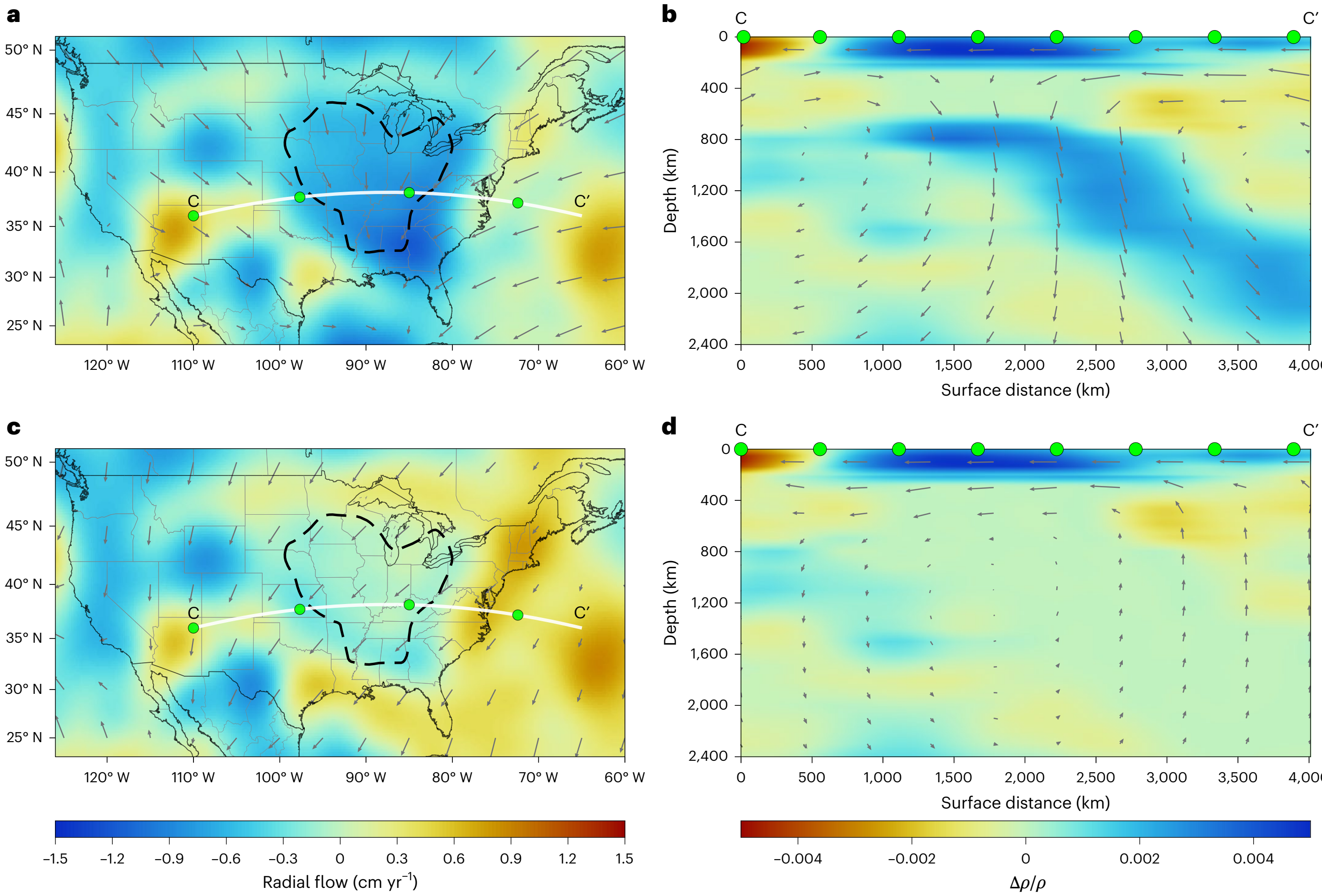

Fig. 3 | Mantle flow induced by the subducting Farallon slab. a, The radial flow speed between depths of 300 and 500 km when the Farallon slab is present. Colours show radial flow, so a negative value represents flow to deeper depths. Arrows show the average horizontal flow fields at the same depth range. The black dashed line is the same as in Fig. 2c. **b**, Cross-section of the input density (ρ) anomaly that drives the mantle flow. Black arrows show the projection of the modelled three-dimensional (3D) flow field on the cross-section. **c**,**d**, As in **a** and **b**, but based on an input model without the Farallon slab. White lines in **a** and **c** show the location of the cross-sections in **c** and **d**, and green geographic markers correspond to those at the top of the cross-sections.

on how far the horizontal flow could attract mobilized materials from surrounding regions, the total thinning associated with the currently imaged anomaly may be of the order of 20–60 km.

Because the dripping material appears more cratonic than ambient mantle in composition, its effective negative buoyancy may be reduced[3]. To evaluate whether the flow caused by the Farallon slab is strong enough to pull down these materials, we merged our V_S anomalies from SATONA with global tomography[35] to estimate the effect of different density anomalies (Extended Data Fig. 10). To account for the range of potential densities of the dripping body, we tested different scaling factors between V_S and density (Extended Data Fig. 10), and in one case we make density negatively correlated with velocity for the dripping material, so that they are positively buoyant. Although the sinking speeds are expectedly reduced for this case, the mantle still flows downward at the dripping locations (Extended Data Fig. 10d). This is partly because strong horizontal inflow driven by the Farallon slab always converges at the dripping location. This test shows that the downward dragging force by the slab could overcome any neutral and even small positive buoyancy of lithospheric material once mobilized.

Compound process of craton thinning

Besides the slab dragging force, to enable dripping of cratonic materials, the base of the craton cannot be very rigid, so downward tractions applied by the deep slab and shear at the LAB could indeed mobilize the lithosphere and entrain material. Such a relatively weak lower part of the craton has previously been inferred. For instance, cratonic kimberlite xenoliths from larger depths often show more evidence for deformation than shallower ones[37,38]. Seismically, cratons often consist of two layers, separated by the mid-lithospheric discontinuity[39], as is also evident in some locations in SATONA (Fig. 2a,b), and the lower half can have strong seismic anisotropy (beneath ~110 km in Extended Data Fig. 6) consistent with a higher degree of deformation. If such deformation is recent, this may suggest a lower strength for the deep craton, and/or discontinuities may be mechanically weak. It has also been argued that the lower half of the craton is not always the original lithosphere, and could have experienced reworking[40]. Hence, it is likely that the base of the lithosphere could be weakened[41] (Fig. 4a), dynamically only marginally stable, and subject to deformation when external forces exist. Moreover, with the inclusion of a small amount of high-density minerals such as garnet in the deep part of the craton[10], the dripping could develop more easily.

Besides driving the flow to mobilize the lithosphere mechanically, past subduction could also facilitate sublithospheric convection and lithospheric weakening[42] (Fig. 4a). When subducting slabs enter the MTZ, volatiles can be released due to dehydration and decarbonization[43–46]. Some of these volatiles will then ascend due to mechanisms such as subduction-induced poloidal flow[47] and the breakdown and re-oxidation of hydrous phases[9], reduce the asthenospheric bulk viscosity, and possibly form hydrous-carbonated melts ponded

https://doi.org/10.1038/s41561-025-01671-x

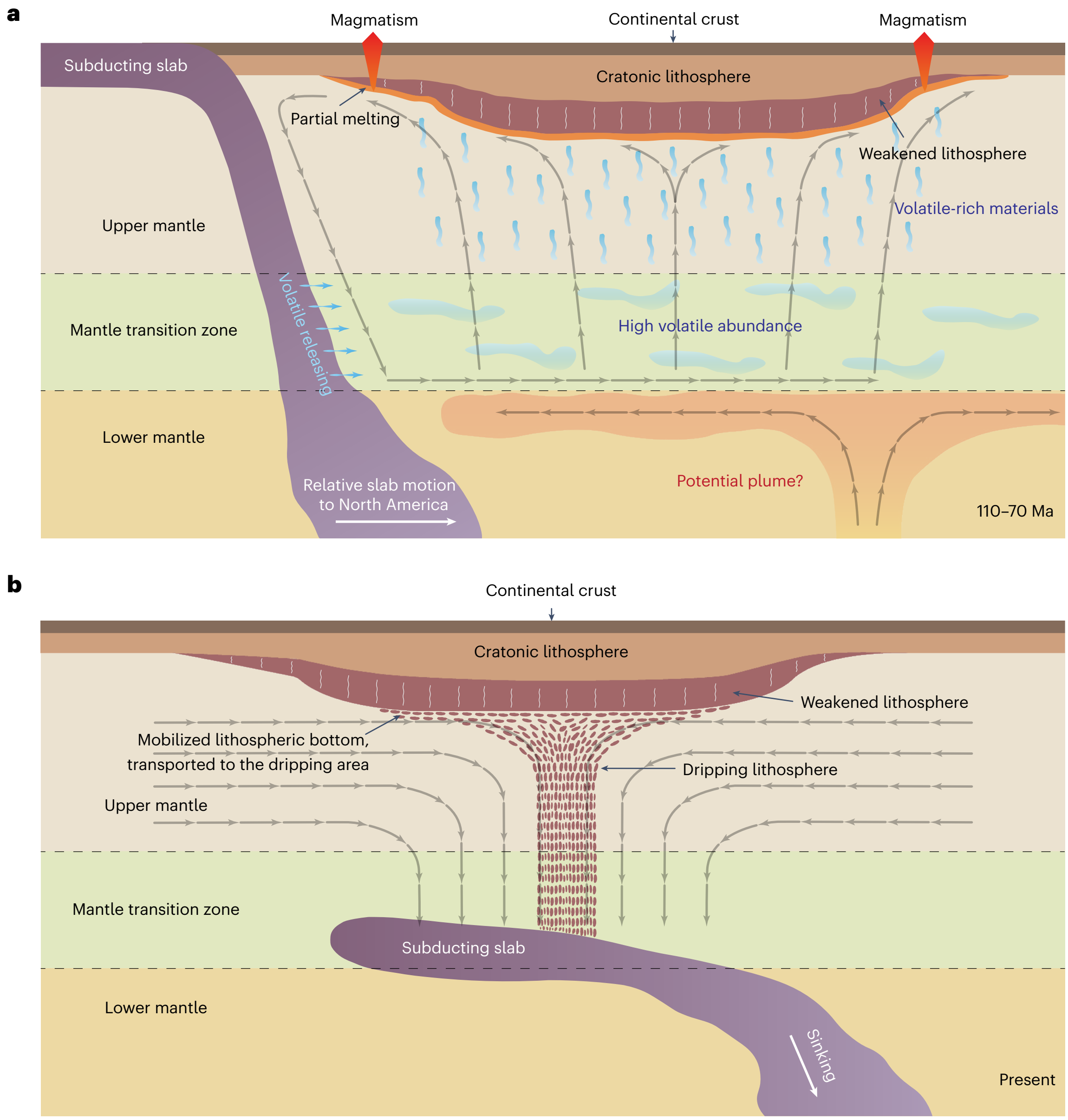

Fig. 4 | Schematics for craton mobilization and thinning. a, Inferred process of successive, slab-induced craton modification. The intrinsic layering of the cratonic lithosphere is depicted. The sequence may involve deep slab motion towards the craton; volatile enrichment in the MTZ; hydration of the asthenosphere; partial melt ponded beneath the craton; magmatism at craton edges; and potential plume-originated materials spreading beneath the MTZ that could later ascend. **b**, Lithospheric dripping mobilized by the deep slab. In **a** and **b**, grey arrows mark large-scale flow lines induced by the slab. The lithosphere drips and mobilized lithospheric bottoms are also depicted.

beneath the LAB[45,46], which could lower the strength of the bottom of the lithosphere.

There is evidence that such subduction-induced weakening has occurred. Relative to North America, the Farallon slab was located further west before ~100 Ma (ref. 32). Around that time, kimberlite, lamproite and carbonatite magmatism occurred at the western edge of the craton (Fig. 1), and such magmatism types favour a carbon-enriched mantle source[45,48]. After 70 Ma, the deep slab moved eastward[32], and kimberlite magmatism appeared near the eastern edge of the craton in Kentucky (Fig. 1). Such findings are consistent with ponded hydrous-carbonated melts (Fig. 4), causing low-V_S anomalies observed at the eastern and western edges of the craton and along the east coast (Figs. 1 and 2a,b).

Past plume activity could also contribute to the weakening. Previous studies suggest hotspot tracks across the continental United States[49,50], which could weaken the lithosphere along their trajectories. When a plume rises up from the lower mantle, the 660-km phase change with a negative Clapeyron slope could temporally stall plume ascent, causing hot materials to pond beneath the MTZ and lead to a transient boundary layer[51] (Fig. 4a), and plume instabilities might then ascend when encountering the Farallon slab, leading to further weakening and thinning of the craton.

We propose that a deep, compositionally distinct craton is being pulled down by slab-induced flow. The small ~60 °C thermal difference of the drips (Fig. 2e) suggests they are probably from the bottom of the craton, which could have been weakened by the processes discussed above. These bottom materials are continuously entrained and mobilized by the slab-induced horizontal flow, which concentrates them in the dripping area (Fig. 3a), where they then follow the downward flow to greater depths. Therefore, compared to delamination, where a large volume of lithosphere is lost locally, the thinning in this study is achieved by constantly mobilizing and removing the bottom of the lithosphere from areas affected by the horizontal flow, which could be larger than the surface projection of the dripping area (Fig. 4b).

Combining all evidence, the lower part of a craton may be weaker and prone to deformation (Fig. 4a). Normally, these weakened portions remain part of the lithosphere due to the lower density, or convective compression effects due to steep LAB gradients[52]. However, if strong tractions from below are present, such as when the slab transitions into the lower mantle, the bottom of the weakened craton may potentially be mobilized and drip into the deeper mantle (Fig. 4b). Although a lower mantle slab anomaly beneath a thick craton is presently only found in North America[35,53], it could have contributed to previous craton-thinning events. This suggests that slabs may not only erode cratons from the sides[4], but craton mobilization and thinning may arise from the deep mantle effects of subduction.

Online content

Any methods, additional references, Nature Portfolio reporting summaries, source data, extended data, supplementary information, acknowledgements, peer review information; details of author contributions and competing interests; and statements of data and code availability are available at https://doi.org/10.1038/s41561-025-01671-x.

References

1. Pearson, D. G. et al. Deep continental roots and cratons. *Nature* **596**, 199–210 (2021).
2. Yuan, H. & Romanowicz, B. Lithospheric layering in the North American craton. *Nature* **466**, 1063–1068 (2010).
3. Jordan, T. H. Structure and formation of the continental tectosphere. *J. Petrol.* **Special_Volume**, 11–37 (1988).
4. Lenardic, A. & Moresi, L. N. Some thoughts on the stability of cratonic lithosphere: effects of buoyancy and viscosity. *J. Geophys. Res.* **104**, 12747–12758 (1999).
5. Gao, S., Rudnick, R. L., Carlson, R. W., McDonough, W. F. & Liu, Y.-S. Re–Os evidence for replacement of ancient mantle lithosphere beneath the North China craton. *Earth Planet. Sci. Lett.* **198**, 307–322 (2002).
6. Lee, C.-T. A., Luffi, P. & Chin, E. J. Building and destroying continental mantle. *Annu. Rev. Earth Planet. Sci.* **39**, 59–90 (2011).
7. Wu, F.-Y., Yang, J.-H., Xu, Y.-G., Wilde, S. A. & Walker, R. J. Destruction of the North China craton in the Mesozoic. *Annu. Rev. Earth Planet. Sci.* **47**, 173–195 (2019).
8. Foley, S. F. Rejuvenation and erosion of the cratonic lithosphere. *Nat. Geosci.* **1**, 503–510 (2008).
9. Liu, L. et al. Mantle dynamics of the North China Craton: new insights from mantle transition zone imaging constrained by P-to-S receiver functions. *Geophys. J. Int.* **231**, 629–637 (2022).
10. Wang, Y. et al. Secular craton evolution due to cyclic deformation of underlying dense mantle lithosphere. *Nat. Geosci.* **16**, 637–645 (2023).
11. Whitmeyer, S. J. & Karlstrom, K. E. Tectonic model for the Proterozoic growth of North America. *Geosphere* **3**, 220–259 (2007).
12. Tappe, S., Smart, K., Torsvik, T., Massuyeau, M. & de Wit, M. Geodynamics of kimberlites on a cooling Earth: clues to plate tectonic evolution and deep volatile cycles. *Earth Planet. Sci. Lett.* **484**, 1–14 (2018).
13. Tao, K., Grand, S. P. & Niu, F. Full-waveform inversion of triplicated data using a normalized-correlation-coefficient-based misfit function. *Geophys. J. Int.* **210**, 1517–1524 (2017).
14. Komatitsch, D., Erlebacher, G., Göddeke, D. & Michéa, D. High-order finite-element seismic wave propagation modeling with MPI on a large GPU cluster. *J. Comput. Phys.* **229**, 7692–7714 (2010).
15. Tromp, J., Komatitsch, D. & Liu, Q. Spectral-element and adjoint methods in seismology. *Commun. Comput. Phys.* **3**, 1–32 (2008).
16. Tao, K., Grand, S. P. & Niu, F. Seismic structure of the upper mantle beneath eastern Asia from full waveform seismic tomography. *Geochem. Geophys. Geosyst.* **19**, 2732–2763 (2018).
17. Bunks, C., Saleck, F. M., Zaleski, S. & Chavent, G. Multiscale seismic waveform inversion. *Geophysics* **60**, 1457–1473 (1995).
18. Bottou, L. Large-scale machine learning with stochastic gradient descent. In *Proc. COMPSTAT'2010: 19th International Conference on Computational Statistics* (eds Lechevallier, Y. & Saporta, G.) 177–186 (Springer, 2010).
19. van Herwaarden, D. P. et al. Accelerated full-waveform inversion using dynamic mini-batches. *Geophys. J. Int.* **221**, 1427–1438 (2020).
20. Hasterok, D. et al. New maps of global geological provinces and tectonic plates. *Earth-Sci. Rev.* **231**, 104069 (2022).
21. Boyce, A. et al. Variable modification of continental lithosphere during the Proterozoic Grenville orogeny: evidence from teleseismic P-wave tomography. *Earth Planet. Sci. Lett.* **525**, 115763 (2019).
22. Schmandt, B. & Lin, F. C. P and S wave tomography of the mantle beneath the United States. *Geophys. Res. Lett.* **41**, 6342–6349 (2014).
23. Sigloch, K. Mantle provinces under North America from multifrequency *P* wave tomography. *Geochem. Geophys. Geosyst.* https://doi.org/10.1029/2010GC003421 (2011).
24. Liang, X., Zhao, D., Hua, Y. & Xu, Y. G. Seismic anisotropy tomography and mantle dynamics of central-eastern USA. *J. Geophys. Res.* **127**, e2022JB025484 (2022).
25. Wang, H., Zhao, D., Huang, Z. & Wang, L. Tomography, seismotectonics, and mantle dynamics of central and eastern United States. *J. Geophys. Res.* **124**, 8890–8907 (2019).
26. McDonough, W. F. & Sun, S.-S. The composition of the Earth. *Chem. Geol.* **120**, 223–253 (1995).
27. Connolly, J. The geodynamic equation of state: what and how. *Geochem. Geophys. Geosyst.* https://doi.org/10.1029/2009GC002540 (2009).
28. Stixrude, L. & Lithgow-Bertelloni, C. Thermal expansivity, heat capacity and bulk modulus of the mantle. *Geophys. J. Int.* **228**, 1119–1149 (2022).
29. Yamauchi, H. & Takei, Y. Polycrystal anelasticity at near-solidus temperatures. *J. Geophys. Res.* **121**, 7790–7820 (2016).
30. Biryol, C. B., Wagner, L. S., Fischer, K. M. & Hawman, R. B. Relationship between observed upper mantle structures and recent tectonic activity across the Southeastern United States. *J. Geophys. Res.* **121**, 3393–3414 (2016).
31. Garrity, C. P. & Soller, D. R. *Database of the Geologic Map of North America: Adapted from the Map by J.C. Reed, Jr. and Others (2005)* Report no. 424 (USGS, 2009); https://pubs.usgs.gov/publication/ds424
32. Straume, E. O., Steinberger, B., Becker, T. W. & Faccenna, C. Impact of mantle convection and dynamic topography on the Cenozoic paleogeography of Central Eurasia and the West Siberian Seaway. *Earth Planet. Sci. Lett.* **630**, 118615 (2024).
33. Schutt, D. & Lesher, C. Effects of melt depletion on the density and seismic velocity of garnet and spinel lherzolite. *J. Geophys. Res.* https://doi.org/10.1029/2003JB002950 (2006).
34. Hager, B. H. & O'Connell, R. J. A simple global model of plate dynamics and mantle convection. *J. Geophys. Res.* **86**, 4843–4867 (1981).
35. Lu, C., Grand, S. P., Lai, H. & Garnero, E. J. TX2019slab: a new *P* and *S* tomography model incorporating subducting slabs. *J. Geophys. Res.* **124**, 11549–11567 (2019).
36. Forte, A. M., Mitrovica, J. X., Moucha, R., Simmons, N. A. & Grand, S. P. Descent of the ancient Farallon slab drives localized mantle flow below the New Madrid seismic zone. *Geophys. Res. Lett.* https://doi.org/10.1029/2006GL027895 (2007).

37. Bascou, J. et al. Seismic velocities, anisotropy and deformation in Siberian cratonic mantle: EBSD data on xenoliths from the Udachnaya kimberlite. *Earth Planet. Sci. Lett.* **304**, 71–84 (2011).
38. Kopylova, M. G., Russell, J. K. & Cookenboo, H. Petrology of peridotite and pyroxenite xenoliths from the Jericho kimberlite: implications for the thermal state of the mantle beneath the Slave Craton, Northern Canada. *J. Petrol.* **40**, 79–104 (1999).
39. Abt, D. L. et al. North American lithospheric discontinuity structure imaged by *Ps* and *Sp* receiver functions. *J. Geophys. Res.* https://doi.org/10.1029/2009JB006914 (2010).
40. Hu, J. et al. Modification of the Western Gondwana craton by plume–lithosphere interaction. *Nat. Geosci.* **11**, 203–210 (2018).
41. Liu, L. & Gao, S. S. Lithospheric layering beneath the contiguous United States constrained by *S*-to-*P* receiver functions. *Earth Planet. Sci. Lett.* **495**, 79–86 (2018).
42. Wang, Z., Kusky, T. M. & Capitanio, F. A. Lithosphere thinning induced by slab penetration into a hydrous mantle transition zone. *Geophys. Res. Lett.* **43**, 11,567–11,577 (2016).
43. Komabayashi, T., Omori, S. & Maruyama, S. Petrogenetic grid in the system MgO-SiO_2-H2O up to 30 GPa, 1600°C: applications to hydrous peridotite subducting into the Earth's deep interior. *J. Geophys. Res.* https://doi.org/10.1029/2003JB002651 (2004).
44. Richard, G., Bercovici, D. & Karato, S.-I. Slab dehydration in the Earth's mantle transition zone. *Earth Planet. Sci. Lett.* **251**, 156–167 (2006).
45. Pokhilenko, N., Agashev, A., Litasov, K. & Pokhilenko, L. Carbonatite metasomatism of peridotite lithospheric mantle: implications for diamond formation and carbonatite-kimberlite magmatism. *Russ. Geol. Geophys.* **56**, 280–295 (2015).
46. Zhang, Y., Wang, C. & Jin, Z. Decarbonation of stagnant slab in the mantle transition zone. *J. Geophys. Res.* **125**, e2020JB019533 (2020).
47. Yang, J. & Faccenda, M. Intraplate volcanism originating from upwelling hydrous mantle transition zone. *Nature* **579**, 88–91 (2020).
48. Sun, C. & Dasgupta, R. Slab–mantle interaction, carbon transport and kimberlite generation in the deep upper mantle. *Earth Planet. Sci. Lett.* **506**, 38–52 (2019).
49. Chu, R., Leng, W., Helmberger, D. V. & Gurnis, M. Hidden hotspot track beneath the eastern United States. *Nat. Geosci.* **6**, 963–966 (2013).
50. Cox, R. T. & Van Arsdale, R. B. The Mississippi Embayment, North America: a first order continental structure generated by the Cretaceous superplume mantle event. *J. Geodyn.* **34**, 163–176 (2002).
51. Dongmo Wamba, M., Montagner, J.-P. & Romanowicz, B. Imaging deep-mantle plumbing beneath La Réunion and Comores hot spots: vertical plume conduits and horizontal ponding zones. *Sci. Adv.* **9**, eade3723 (2023).
52. Paul, J., Conrad, C. P., Becker, T. W. & Ghosh, A. Convective self-compression of cratons and the stabilization of old lithosphere. *Geophys. Res. Lett.* **50**, e2022GL101842 (2023).
53. French, S. W. & Romanowicz, B. Broad plumes rooted at the base of the Earth's mantle beneath major hotspots. *Nature* **525**, 95–99 (2015).

Methods

Seismic full-waveform adjoint tomography

Seismograms were obtained for 206 earthquakes occurring between 2004 and 2021, at 6,099 individual stations (Extended Data Fig. 1). Their magnitudes were mainly between 5.5 and 6.8 (thus avoiding low-quality data and satisfying the point source assumption, which is often not valid for larger earthquakes[16]). All 206 earthquakes were used during the coarse-grid stage, which took 126 iterations. Of those earthquakes, 110 were selected for the following 90-iteration fine-grid stage (Extended Data Fig. 1). Due to strong noise on the horizontal components, only vertical components were used for ocean-bottom seismometers, and both tilt and compliance noise were removed[54].

We used multiple body wave phases, including P, S, PP, SS, PPP and SSS, and their depth phases, as well as surface waves. For each body wave phase, we cut a waveform segment starting 30 s before and ending 50 s after the arrival time for waveform fitting. During the coarse-grid stage, body waves were filtered between 17 and 100 s, and for the fine-grid stage, the filter was 14–100 s. Rayleigh and Love waves were filtered in multiple period bands, including 20–40 s, 40–60 s, 60–80 s and 80–150 s. Waveform segments were also cut for surface waves to contain their full envelopes. In total, we used 1.5×10^6 waveform segments.

The inversion scheme is similar to the one in ref. 16. During inversion, we tried to maximize the correlation coefficient between the synthetic and observed waveforms, which guides the velocity structure to fit phase shapes, while not being strongly affected by less constrained factors such as attenuation. Furthermore, compared to methods based purely on travel times, this method can exploit more information in the detailed shape of waveforms. A preconditioned conjugate gradient method is used to update the model[16], and a diagonal Hessian is approximated by calculating the sensitivity kernel difference after perturbing the model[55]. Weights for different segments are based on four metrics: correlation coefficients, maximum cross-correlation values, time differences between synthetic and observed arrivals, and the signal-to-noise ratio of the observations[16]. In this study, a segment is weighted as unity when these four criteria are met: correlation coefficient > 0.8, maximum cross-correlation value > 0.95, time shift < 4 s and signal-to-noise ratio > 12; in contrast, it is weighted as zero if one of these criteria is met: correlation coefficient < 0.55, maximum cross-correlation value < 0.7, time shift > 8 s or signal-to-noise ratio < 8. For metrics lying between these thresholds, the weight is determined by the cosine-shape function in ref. 16.

To overcome the cost of wavefield simulations, which often limits adjoint tomography to a few tens of iterations[16,55], and to reduce the possibility of being trapped in local minima, we included a mini-batch algorithm by using only a portion of earthquakes for each iteration. This algorithm is commonly used for stochastic gradient descent in machine learning[18]. This algorithm is similar to the one in ref. 19, where mini-batches greatly enhance the convergence rate by reducing the redundancy among sensitivity kernels from different earthquakes. However, unlike ref. 19, the Hessian is not estimated via the L-BFGS algorithm[56], so we do not need to worry about the positive definiteness of the Hessian during mini-batch selection. Hence, there only remain two key procedures for mini-batch selection: (1) choosing earthquakes to be excluded for the next iteration; (2) adding earthquakes not used in the current iteration.

We used a similar algorithm to that in ref. 19 to select earthquakes to be excluded. The angular distance between the summed kernel using all earthquakes in the current iteration and the summed kernel for all preserved earthquakes with one earthquake removed is calculated, and the earthquake with the smallest angular distance is removed. Such earthquake exclusion is performed iteratively[19] until the angular distance reaches 30° or the total number of excluded stations exceeds 55% of the earthquakes used for the current iteration.

The way to add new earthquakes for the next iteration is more stochastic to avoid some earthquakes being constantly chosen. Specifically, we give each candidate earthquake a probability based on (1) the average distance from a candidate earthquake to its three nearest earthquakes that have secured a spot for the next iteration and (2) the number of iterations that this earthquake was used in. Hence, earthquakes either far from other earthquakes or not frequently used have a better chance of being selected.

We used model US22[57] as our starting structure. To account for attenuation, we used the 3D attenuation model QRFSI12[58]; although SpecFem3D Globe handles attenuation with a constant Q across frequencies[59], the velocities shown in this study are for 1 s. We used CRUST1.0[60] for Moho topography, and S362ANI[61] for the topography of the 410 and 660 discontinuities.

Accurate earthquake sources are crucial for tomography. In this study, we inverted all source parameters[16] within the gCMT solution[62] before inverting for structure, or once the structure inversion had produced substantial updates from the model used for the last source inversion. Sources were updated eight times; each time, the number of iterations for different earthquakes depends on their convergence rates. Meanwhile, to overcome the uneven distribution of stations, in addition to the original weight based on the four metrics, the weight for a certain station was further normalized by the sum of weights for all stations around it with an azimuth difference of <7.5° and epicentral distance difference of <6°. A water level of 2‰ the summed weight of all stations was applied during normalization to not overweight isolated stations.

The forward and adjoint simulations for both structural and source inversions were performed using SpecFem3D Globe v8.0.0[14] on a server with four Nvidia A100 GPUs. For each earthquake, the duration of simulated wavefields is determined by the end time of the 20–40-s Rayleigh wave segment at the farthest station. The simulation domain has a dimension of 57° × 79° (Extended Data Fig. 1), and during the more influential fine-grid stage, the horizontal element size is ~44 km on the free surface, setting the spacing between Gauss–Lobatto–Legendre interpolation points as ~11 km, with a minimum resolved period of 11 s.

In this Article we mainly focus on isotropic velocity anomalies. During simulations, we made the structure isotropic below the 410 discontinuity, and transversely isotropic above it. Hence, both isotropic velocity and radial anisotropy were solved for during inversion, and we used the Voigt average[63] to approximate the isotropic velocity. To compare velocity anomalies at different depths, seismic velocities are shown as velocity perturbations with respect to a reference model. A one-dimensional (1D) mantle reference model for V_S and V_P is obtained by averaging the final velocity model for all regions with good resolution (Extended Data Fig. 6), and in the crust, 3D velocities from CRUST1.0[60] are assumed as the reference.

Resolution tests of the model

Two resolution tests were performed separately for V_S and V_P (Extended Data Fig. 5). In each test, the same point-shape velocity perturbations were added to the final $\Delta V_S/V_S$ and $\Delta V_P/V_P$ models. These perturbations are horizontally 4° and vertically 200-km apart from each other, and there is reversed polarization between neighbours (Extended Data Fig. 5). The maximum amplitude of the perturbations is 0.01, and their shapes are characterized by a Gaussian with a standard deviation of 40 km. Such a spatial extent is comparable with the wavelength of body waves used in this study, making the test challenging and, as set up, preferable to checkerboard tests[64].

During the test, we generated waveforms for the perturbed model as 'observations', then started from the unperturbed model to invert for the perturbations. Meanwhile, to resemble the resolution of real data, we used the same set of weighting for waveform segments as in the last tomography iteration. Due to computation resources, we did not replicate the 206 iterations for tomography, but 16 iterations were still performed for each test with the mini-batch strategy (Extended Data Fig. 5). Compared to commonly used one-iteration tests for full-waveform tomography[16,55], this multi-iteration test refines structures at places with lower data coverage to better indicate the actual resolution.

A specific test was also designed for the resolution on the high-V_S dripping bodies (Extended Data Fig. 7). Here, due to computation limits, we used the point-spread function method[16,65] with one iteration. We first made a model with all high-V_S anomalies around the dripping region removed, then calculated the V_S sensitivity kernel for this modified model. After that, we obtained the difference in preconditioned V_S sensitivity kernel between the original model and the modified one, which represents the V_S change that the data would favour to compensate for the removed dripping body.

Based on results from these tests, the dripping bodies are not likely to be artefacts based on their geometries. Although the general shape of these bodies is subvertical, they also contain secondary features that are horizontally aligned (Fig. 2a,b), which cannot be produced by smearing along ray paths, and the resolution test shows no distortion of structures around the region (Extended Data Fig. 5). Also, given the earthquake-station distribution (Extended Data Fig. 1), there are no ray paths following the eastward dripping direction of high-V_S bodies on the east side (Fig. 2b).

Composition and temperature estimation

Because there are two observables (V_S and V_P), and temperature is one variable to be constrained, only one compositional variable can be solved for, so we modelled compositions between two endmembers. Endmember compositions are expressed as oxide weight percentages for the SiO_2–Al_2O_3–MgO–FeO–CaO–Na_2O system. We took one endmember to be pyrolite following ref. 26, with SiO_2 = 45%, Al_2O_3 = 4.45%, MgO = 37.8%, FeO = 8.05%, CaO = 3.55% and Na_2O = 0.36%. For the endmember composition of a depleted cratonic mantle lithosphere, we compiled whole rock major element compositions for peridotite xenolith samples from four cratons (Extended Data Fig. 9): Greenland[66–68], Slave[69], Kaapvaal[70–72] and Siberia[73–75]. Based on these samples, clear negative correlations are seen between the Mg number (Mg# = 100 × Mg/(Mg + Fe)) and the FeO content, MgO and SiO_2 content, MgO and Al_2O_3 content and MgO and CaO content, and all these relationships could be generalized through linear regression (Extended Data Fig. 9). Therefore, by setting the Mg# to 93.7 for the craton endmember, we can get a corresponding FeO from the first relationship, and a MgO content is obtained based on that Mg# and FeO. With the MgO, based on other relationships, other major element contents can be determined. The amount of Na_2O is very small and can be ignored. Together, the craton endmember has SiO_2 = 46.55%, Al_2O_3 = 1.1%, MgO = 45.99%, FeO = 5.7% and CaO = 0.62%.

With these endmember compositions, we estimated the dependence of $\Delta V_S/V_S$ and $\Delta V_P/V_P$ on composition and temperature at different depths. We performed the conversion between 200- and 380-km depths, because dripping bodies are clearly observed there (Extended Data Fig. 3), the depth is not so deep as to be affected by potential inaccuracy from the assumed 410-discontinuity topography, and $\Delta V_P/V_P$ is best resolved at a depth of ~300 km (Extended Data Fig. 5).

To estimate the temperature dependence, we calculated seismic velocities under different temperature and pressure conditions. We assumed an ambient mantle potential temperature of 1,350 °C (ref. 76) and an adiabatic temperature gradient of 0.4 °C km^{-1} (ref. 77). At each depth, we estimated the elastic V_S and V_P 50 °C above and below the adiabat using Perple_X[27] with thermodynamic data and solutions in ref. 28, and pressures from PREM[78]. We then estimated the anelasticity effect for these two temperatures at a period of 20 s based on the relationship in ref. 29 through the very-broadband rheology calculator[79] with the solidus from ref. 80 assumed for the calculation in ref. 29. We assumed the attenuation effect on the bulk modulus to be negligible, and how complex anelastic compliance in ref. 29 would affect V_P was derived in the same way as in ref. 81 for V_S. The period of 20 s was chosen as it is close to the frequency of body waves used in this study. Next, gradients of V_S and V_P with respect to temperature were obtained by calculating the differences in anelastic V_S and V_P between these two temperatures and dividing them by the temperature difference of 100 °C. These gradients were further divided by the anelastic V_S and V_P at adiabatic temperatures (labelled g_β^T and g_α^T) for further conversion.

The compositional dependence was estimated similarly. By assuming mechanical mixing[82], at different depths along the assumed 1,350 °C adiabat we calculated the difference in anelastic V_S and V_P between the two endmember compositions, and these differences were divided by unity to represent the compositional gradients. These gradients of V_S and V_P were then divided by the 1D reference V_S and V_P of SATONA (Extended Data Fig. 6) at these depths (labelled as g_β^f and g_α^f) for conversion.

V_S and V_P perturbations were then converted to temperature and compositional perturbations. Here, we convert velocity perturbations rather than absolute velocities, because absolute velocities could be strongly influenced by the assumed reference anelasticity model and the exact composition of the mantle rocks, whereas perturbations are less dependent on these reference conditions. Before conversion, to avoid misalignment of independently constrained V_S and V_P features, $\Delta V_S/V_S$ and $\Delta V_P/V_P$ were smoothed by convolving with a 3D Gaussian, whose horizontal and vertical standard deviations were 120 km and 20 km. Velocities were also converted to 20 s based on the attenuation model[58] for consistency. Velocity perturbations were expressed by temperature perturbation (ΔT) and compositional perturbation (Δf) as $\Delta V_S/V_S = g_\beta^T \Delta T + g_\beta^f \Delta f$ and $\Delta V_P/V_P = g_\alpha^T \Delta T + g_\alpha^f \Delta f$, and ΔT and Δf were obtained by solving these two equations (Fig. 2d,e and Extended Data Fig. 9). When converting for the dripping anomalies (for example, Fig. 2d,e), only geographic locations within the dripping area with positive $\Delta V_S/V_S$ and $\Delta V_P/V_P$ were considered.

The range of converted compositional perturbation appears to be large for the whole model (Extended Data Fig. 9i,m). However, these endmember compositions might not be suitable for other areas, and the anelasticity model could be more complicated for hot environments[29] such as in the western United States and Mexico (Extended Data Fig. 3). As our goal is mainly to show whether the overall V_S and V_P patterns for dripping bodies could correspond to an increased amount of cratonic material, we focused more on the relative compositional difference between the dripping area and regions excluding the dripping area, rather than the exact values.

Estimation of thinning

An approximate estimate of the amount of lithospheric thinning follows from assuming that the amount of cratonic material is proportional to $\Delta V_S/V_S$, and all previously dripped lithosphere is still present in the tomographic model as fast anomalies. We first set $\Delta V_S/V_S$ at 180 km as a reference for craton material, as this is within the craton, but not too shallow to be strongly influenced by cold temperature. We then calculated the sum of positive $\Delta V_S/V_S$ in the dripping area (Fig. 2c) between depths of 250 and 550 km and obtained the ratio between them and the reference summed $\Delta V_S/V_S$ at 180 km, which represents the volume proportion of cratonic materials at those depths and is on average ~20%. Hence, the thinning would be (550 km − 250 km) × 20% = 60 km if dripping locally. If horizontal flow induced by the slab (Fig. 3a versus 3c) were able to focus material from the whole cratonic region covered by this model (Fig. 1) with an area of ~4 × 10^6 km^2, given the dripping area has an area of ~1.5 × 10^6 km^2 (~38% of the cratonic area), the average amount of thinning would be calculated to be 60 km × 38% ≈ 23 km. Hence, the actual thinning amount is probably 20–60 km. However, some regions may experience more thinning than others; for instance, flanks at the western edge of the craton in Fig. 2a,b could partly be caused by the thinning. Meanwhile, although we have estimated compositional perturbation, and it is a powerful way to show the substantial distinction in composition, we did not use it for the thinning estimation, as what are obtained are perturbations with large uncertainties that are also subject to many assumptions.

Geodynamic modelling of mantle convection

Mantle flow fields driven by different density structures were modelled. The calculation was based on refs. 34,83 up to spherical harmonic degree 63. The 1D viscosity distribution from ref. 84 and the surface MORVEL[85] plate motion were assumed, and we only considered vertical variations in viscosity, for simplicity, which led us to trust patterns more than amplitudes of flow (for example, ref. 86).

We first estimated the flow fields from two density models based on the global tomographic model TX2019slab[35]. Starting from its V_S model, we removed all velocity perturbations around the dripping area at depths of 280–600 km (Fig. 3b,d) to eliminate local buoyancy flows. For one model, at each depth slice below 600 km, we then outlined the geometry of the high-velocity Farallon slab and removed all perturbations within it (Fig. 3d). After that, two V_S models with or without the Farallon slab were converted to density based on a V_S–density relationship[84], and their corresponding flow fields were calculated (Fig. 3).

To evaluate whether the downward flow induced by the Farallon slab was strong enough to drag down the dripping materials, we calculated flow fields after merging SATONA with TX2019slab. For SATONA, we only used reliable regions based on resolution tests (Extended Data Fig. 5). For locations >200 km within the resolution boundary (Extended Data Fig. 5), $\Delta V_S/V_S$ from SATONA was used, and for locations >200 km outside the boundary, TX2019slab[35] was used. For locations within 200 km of the boundary, we weighted the averaged $\Delta V_S/V_S$ between these two models to make the merged model continuous at ±200 km from the boundary. A similar merging strategy was designed for the bottom of SATONA for depths <700 km, while using TX2019slab[35] velocity for depths >900 km. In between, weighted averaged values were used. After smoothing, the $\Delta V_S/V_S$ of the dripping area was ~1% (Extended Data Fig. 9e), in agreement with some previous longer-wavelength models (Extended Data Fig. 7). To understand how dripping-body densities could affect flows, we tested four scenarios by setting the V_S–density scaling factor at depths of 260–600 km for positive V_S anomalies within the dripping area to be 1, 0.5, 0 and −0.5 times the factor for the rest of the region[84] (Extended Data Fig. 10); in the last scenario, this made the dripping bodies positively buoyant (Extended Data Fig. 10d).

We also used past slab locations to help our interpretation (Fig. 1). Mantle structures in history were predicted in ref. 32 by advecting velocity structures in TX2019slab[35] back in time. Because the present-day Farallon slab does not always appear above the 660 discontinuity, we chose to use the contour of the 0.12% density anomaly at 800-km depth to outline the slab for those palaeo-density models. Then, to show the relative location of the Farallon slab to the North American plate, these outlines were translated to their present location based on the assumed plate motion[87] in ref. 32. These past slab locations were analysed with dated magmatism (Fig. 1) in Kansas[88], Arkansas[89], Monroe uplift[90], Kentucky[91] and Virginia[92].

Data availability

Seismograms from networks other than the Mexican National Network were downloaded from the IRIS Data Management Center (http://ds.iris.edu/ds/nodes/dmc/). Seismograms from the Mexican National Network (https://doi.org/10.21766/SSNMX/SN/MX) were downloaded via the SSNstp client, which is free (http://www2.ssn.unam.mx:8080/getData/SSNdata_UseAndPolicy.pdf) upon request without requirements for authorization. The SATONA model is deposited in the IRIS archive (https://ds.iris.edu/ds/products/emc-earthmodels/), which also hosts US-SL-2014[22], CAP22[93], BBNAP19[21] and NA13[94], which were compared. For other compared models, US22[57] is available on H. Zhu's website (https://labs.utdallas.edu/seismic-imaging-lab/download/), and models in refs. 23,25 are available as a supplement in their publications. All figures and maps are generated using Generic Mapping Tools[95].

Code availability

Computer codes used for data processing, inversion, composition analysis and plotting are available upon request. SpecFem3D Globe and the geodynamic tool to calculate the flow field are openly available on GitHub (https://github.com/SPECFEM/specfem3d_globe, https://github.com/geodynamics/hc).

References

54. Janiszewski, H. A., Gaherty, J. B., Abers, G. A., Gao, H. & Eilon, Z. C. Amphibious surface-wave phase-velocity measurements of the Cascadia subduction zone. *Geophys. J. Int.* **217**, 1929–1948 (2019).
55. Zhu, H., Bozdağ, E. & Tromp, J. Seismic structure of the European upper mantle based on adjoint tomography. *Geophys. J. Int.* **201**, 18–52 (2015).
56. Liu, D. C. & Nocedal, J. On the limited memory BFGS method for large scale optimization. *Math. Program.* **45**, 503–528 (1989).
57. Zhu, H., Komatitsch, D. & Tromp, J. Radial anisotropy of the North American upper mantle based on adjoint tomography with USArray. *Geophys. J. Int.* **211**, 349–377 (2017).
58. Dalton, C. A., Ekström, G. & Dziewoński, A. M. The global attenuation structure of the upper mantle. *J. Geophys. Res.* https://doi.org/10.1029/2007JB005429 (2008).
59. Komatitsch, D. & Tromp, J. Spectral-element simulations of global seismic wave propagation—I. Validation. *Geophys. J. Int.* **149**, 390–412 (2002).
60. Laske, G., Masters, G., Ma, Z. & Pasyanos, M. Update on CRUST1.0—a 1-degree global model of Earth's crust. *Geophys. Res. Abstr.* **15**, EGU2013-2658 (2013).
61. Kustowski, B., Ekström, G. & Dziewoński, A. Anisotropic shear-wave velocity structure of the Earth's mantle: a global model. *J. Geophys. Res.* https://doi.org/10.1029/2007JB005169 (2008).
62. Ekström, G., Nettles, M. & Dziewoński, A. The global CMT project 2004–2010: centroid-moment tensors for 13,017 earthquakes. *Phys. Earth Planet. Inter.* **200**, 1–9 (2012).
63. Panning, M. & Romanowicz, B. A three-dimensional radially anisotropic model of shear velocity in the whole mantle. *Geophys. J. Int.* **167**, 361–379 (2006).
64. Rawlinson, N. & Spakman, W. On the use of sensitivity tests in seismic tomography. *Geophys. J. Int.* **205**, 1221–1243 (2016).
65. Fichtner, A. & Leeuwen, T. V. Resolution analysis by random probing. *J. Geophys. Res.* **120**, 5549–5573 (2015).
66. Bernstein, S., Kelemen, P. B. & Brooks, C. K. Depleted spinel harzburgite xenoliths in Tertiary dykes from East Greenland: restites from high degree melting. *Earth Planet. Sci. Lett.* **154**, 221–235 (1998).
67. Hanghøj, K., Kelemen, P., Bernstein, S., Blusztajn, J. & Frei, R. Osmium isotopes in the Wiedemann Fjord mantle xenoliths: a unique record of cratonic mantle formation by melt depletion in the Archaean. *Geochem. Geophys. Geosyst.* https://doi.org/10.1029/2000GC000085 (2001).
68. Wittig, N. et al. Origin of cratonic lithospheric mantle roots: a geochemical study of peridotites from the North Atlantic Craton, West Greenland. *Earth Planet. Sci. Lett.* **274**, 24–33 (2008).
69. Liu, J. et al. Plume-driven recratonization of deep continental lithospheric mantle. *Nature* **592**, 732–736 (2021).
70. Griffin, W., Graham, S., O'Reilly, S. Y. & Pearson, N. Lithosphere evolution beneath the Kaapvaal Craton: Re–Os systematics of sulfides in mantle-derived peridotites. *Chem. Geol.* **208**, 89–118 (2004).

71. Simon, N. S., Carlson, R. W., Pearson, D. G. & Davies, G. R. The origin and evolution of the Kaapvaal cratonic lithospheric mantle. *J. Petrol.* **48**, 589–625 (2007).
72. Simon, N. S., Irvine, G. J., Davies, G. R., Pearson, D. G. & Carlson, R. W. The origin of garnet and clinopyroxene in 'depleted' Kaapvaal peridotites. *Lithos* **71**, 289–322 (2003).
73. Boyd, F. et al. Composition of the Siberian cratonic mantle: evidence from Udachnaya peridotite xenoliths. *Contrib. Mineral. Petrol.* **128**, 228–246 (1997).
74. Ionov, D. A., Doucet, L. S. & Ashchepkov, I. V. Composition of the lithospheric mantle in the Siberian craton: new constraints from fresh peridotites in the Udachnaya-East kimberlite. *J. Petrol.* **51**, 2177–2210 (2010).
75. Ionov, D. A., Doucet, L. S., Carlson, R. W., Golovin, A. V. & Korsakov, A. V. Post-Archean formation of the lithospheric mantle in the central Siberian craton: Re–Os and PGE study of peridotite xenoliths from the Udachnaya kimberlite. *Geochim. Cosmochim. Acta* **165**, 466–483 (2015).
76. Herzberg, C. & Gazel, E. Petrological evidence for secular cooling in mantle plumes. *Nature* **458**, 619–622 (2009).
77. Katsura, T. A revised adiabatic temperature profile for the mantle. *J. Geophys. Res.* **127**, e2021JB023562 (2022).
78. Dziewonski, A. M. & Anderson, D. L. Preliminary reference Earth model. *Phys. Earth Planet. Inter.* **25**, 297–356 (1981).
79. Havlin, C., Holtzman, B. K. & Hopper, E. Inference of thermodynamic state in the asthenosphere from anelastic properties, with applications to North American upper mantle. *Phys. Earth Planet. Inter.* **314**, 106639 (2021).
80. Hirschmann, M. M. Mantle solidus: experimental constraints and the effects of peridotite composition. *Geochem. Geophys. Geosyst.* https://doi.org/10.1029/2000GC000070 (2000).
81. McCarthy, C., Takei, Y. & Hiraga, T. Experimental study of attenuation and dispersion over a broad frequency range: 2. The universal scaling of polycrystalline materials. *J. Geophys. Res.* https://doi.org/10.1029/2011JB008384 (2011).
82. Xu, W., Lithgow-Bertelloni, C., Stixrude, L. & Ritsema, J. The effect of bulk composition and temperature on mantle seismic structure. *Earth Planet. Sci. Lett.* **275**, 70–79 (2008).
83. Hager, B. H., O'Connell, R. J., Steinberger, B. & Becker, T. HC v1.0.15 (Computational Infrastructure for Geodynamics, 2022).
84. Steinberger, B. & Calderwood, A. R. Models of large-scale viscous flow in the Earth's mantle with constraints from mineral physics and surface observations. *Geophys. J. Int.* **167**, 1461–1481 (2006).
85. DeMets, C., Gordon, R. G. & Argus, D. F. Geologically current plate motions. *Geophys. J. Int.* **181**, 1–80 (2010).
86. Ghosh, A., Becker, T. & Humphreys, E. Dynamics of the North American continent. *Geophys. J. Int.* **194**, 651–669 (2013).
87. Torsvik, T. H. et al. Pacific-Panthalassic reconstructions: overview, errata and the way forward. *Geochem. Geophys. Geosyst.* **20**, 3659–3689 (2019).
88. Blackburn, T. J., Stockli, D. F., Carlson, R. W. & Berendsen, P. (U–Th)/He dating of kimberlites—a case study from north-eastern Kansas. *Earth Planet. Sci. Lett.* **275**, 111–120 (2008).
89. Eby, G. N. & Vasconcelos, P. Geochronology of the Arkansas alkaline province, southeastern United States. *J. Geol.* **117**, 615–626 (2009).
90. Baksi, A. K. The timing of Late Cretaceous alkalic igneous activity in the northern Gulf of Mexico basin, southeastern USA. *J. Geol.* **105**, 629–644 (1997).
91. Heaman, L. M., Kjarsgaard, B. A. & Creaser, R. A. The temporal evolution of North American kimberlites. *Lithos* **76**, 377–397 (2004).
92. Zartman, R. E. Geochronology of some alkalic rock provinces in eastern and central United States. *Annu. Rev. Earth Planet. Sci.* **5**, 257–286 (1977).
93. Boyce, A. et al. A new *P*-wave tomographic model (CAP22) for North America: implications for the subduction and cratonic metasomatic modification history of western Canada and Alaska. *J. Geophys. Res.* **128**, e2022JB025745 (2023).
94. Bedle, H., Lou, X. & van der Lee, S. High-resolution imaging of continental tectonics in the mantle beneath the United States, through the combination of USArray data sets. Preprint at ESS Open Archive https://doi.org/10.1002/essoar.10506069.1 (2022).
95. Wessel, P. et al. The generic mapping tools version 6. *Geochem. Geophys. Geosyst.* **20**, 5556–5564 (2019).
96. Kennett, B. L. N., Engdahl, E. R. & Buland, R. Constraints on seismic velocities in the Earth from traveltimes. *Geophys. J. Int.* **122**, 108–124 (1995).

Acknowledgements

We thank R. W. Clayton, X. Pérez Campos and C. Cardenas Monroy for acquiring data from the Mexican National Network. We thank M. Wiederspahn for managing the computation resources and data. We thank Z. Zhao and X. Li for discussions regarding the inversion method. We thank E. Sandvol, C. Sun, D. B. Rowley, E. O. Straume, E. Clennett and E. K. Heilman for constructive discussions on the interpretation of structures. Mexican National Network data were obtained by the Servicio Sismológico Nacional (México), and station maintenance, data acquisition and distribution are thanks to its personnel. S.P.G. was partially supported by NSF EAR-1902400 (S.P.G.), NSF EAR-1903108 (S.P.G.) and the Jackson School of Geosciences. T.W.B. was partially supported by NSF EAR-2045292 (T.W.B.). J.H. was also partially supported by NSF EAR-1902400 and the Jackson School of Geosciences when employed at UT Austin.

Author contributions

J.H. conducted the tomography, data analysis, composition conversion and modelling. S.P.G. advised on the seismological aspects of the study. T.W.B. advised on the geodynamic modelling aspects. J.H., S.P.G. and T.W.B. put together the main conclusions of the paper. H.A.J. processed seismic data from the ocean-bottom seismometers. C.L. helped with the inversion approach. D.T.T. helped with the computational environment. H.Z. advised on the inversion approach. Detailed interpretation of the results reflects discussions among the authors. The paper was written by J.H. with contributions from S.P.G., T.W.B. and other authors.

Competing interests

The authors declare no competing interests.

Additional information

Extended data is available for this paper at https://doi.org/10.1038/s41561-025-01671-x.

Correspondence and requests for materials should be addressed to Junlin Hua.

Peer review information *Nature Geoscience* thanks Lin Liu and the other, anonymous, reviewer(s) for their contribution to the peer review of this work. Primary Handling Editor: Tamara Goldin, in collaboration with the *Nature Geoscience* team.

https://doi.org/10.1038/s41561-025-01671-x

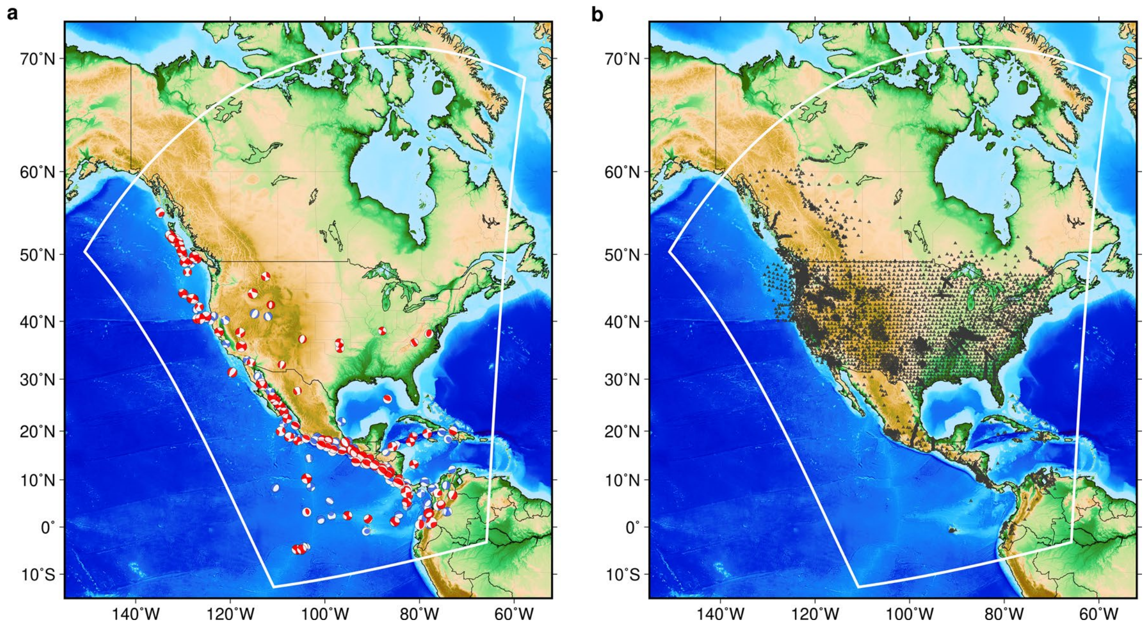

Extended Data Fig. 1 | The distribution of earthquakes and stations. a. Map of earthquakes symbolized by their focal mechanisms after source inversions. Red earthquakes are included during both coarse and fine stages, while blue earthquakes are only used during the coarse stage. The white solid line outlines the simulation domain. **b**. Map of stations (black triangles) used in the inversion.

 https://doi.org/10.1038/s41561-025-01671-x

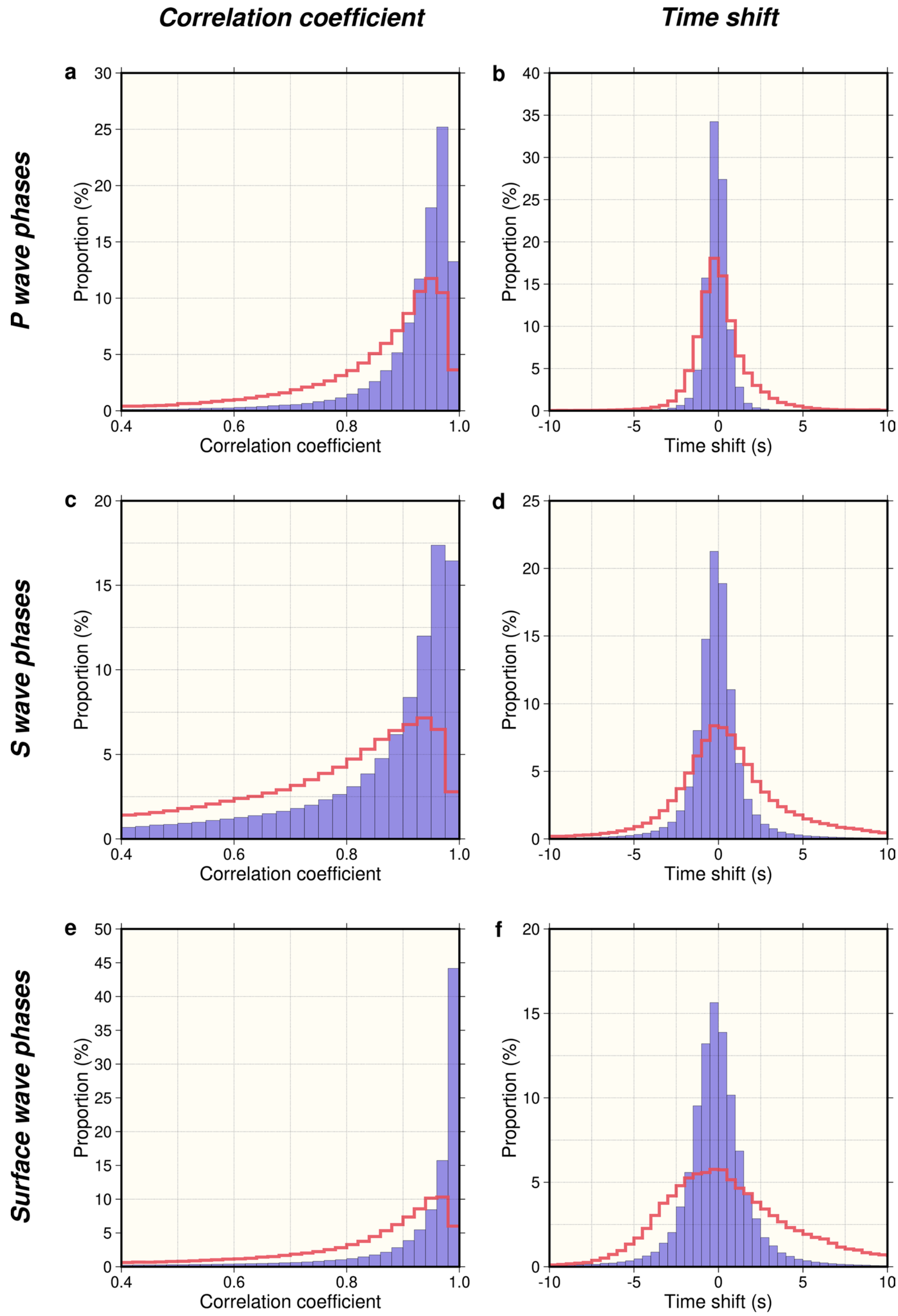

Extended Data Fig. 2 | Improvement on data-fitting through inversion. Figures in the left column (**a**, **c**, and **e**) show the distribution of correlation coefficient between synthetic and observed seismograms before (red line) and after (blue bars) the 206 iterations. Figures in the right column (**b**, **d**, and **f**) are illustrated in the same way, but are for the time shift between synthetic and observed data. The first row is for all P motion related body wave segments (for example, P, PP, etc.); the second row is for S motion related segments (for example, S, SS, etc.); and the third row is for surface wave segments (Rayleigh and Love waves). To be consistent, only the 110 earthquakes that are included in the fine-grid stage are used here, and only segments with signal-to-noise ratio[16] > 8 are counted. Waveforms used for distributions before inversion for the coarse-grid stage (red lines) were filtered at lower frequencies, which are supposed to be easier for data-fitting than ones after inversion (blue bars).

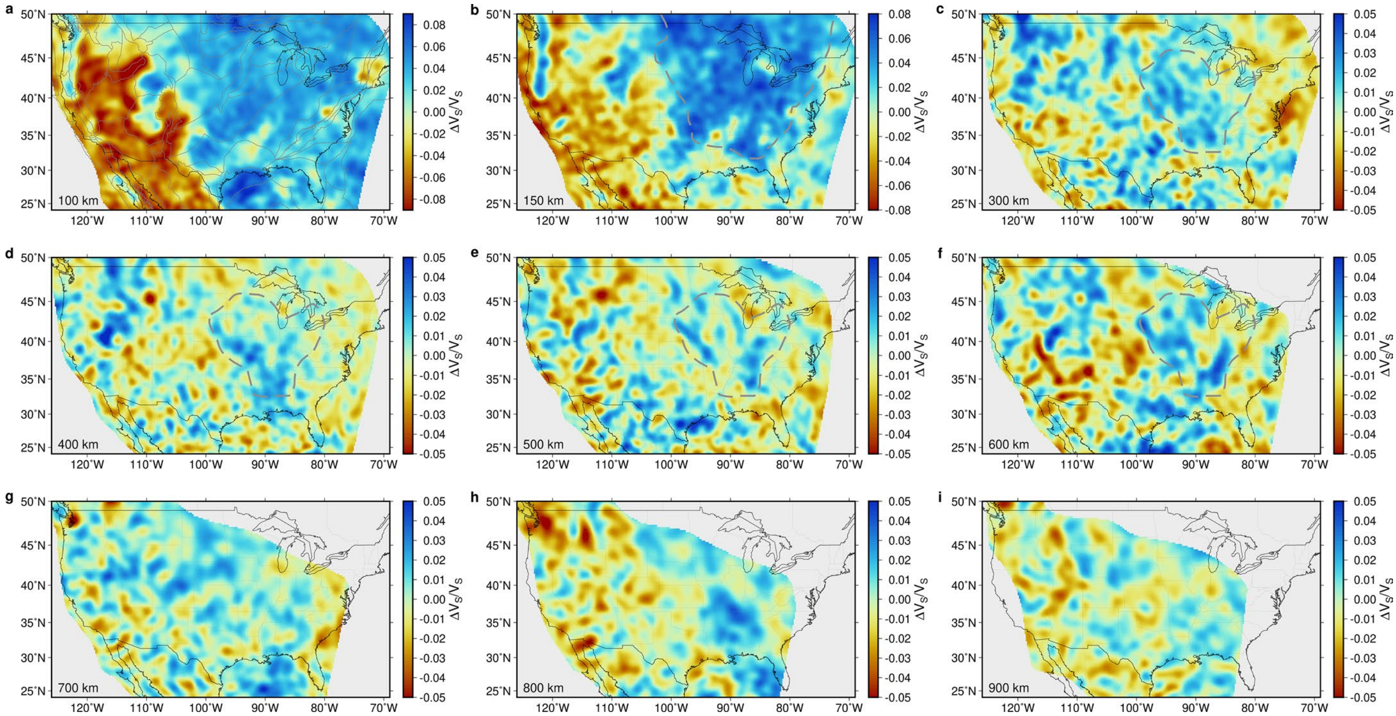

Extended Data Fig. 3 | Isotropic V_S distribution at different depths. a-i. V_S perturbations at 100, 150, 300, 400, 500, 600, 700, 800, and 900 km depths. Only reliable regions (Extended Data Fig. 5) are shown colored (note variable color bars). Tectonic regions[20] are outlined in **a**. The craton boundary in Fig. 1 is plotted as gray dashed lines on **b**. The boundary for dripping bodies in Fig. 2c is plotted as gray dashed lines on **c**-**f**.

https://doi.org/10.1038/s41561-025-01671-x

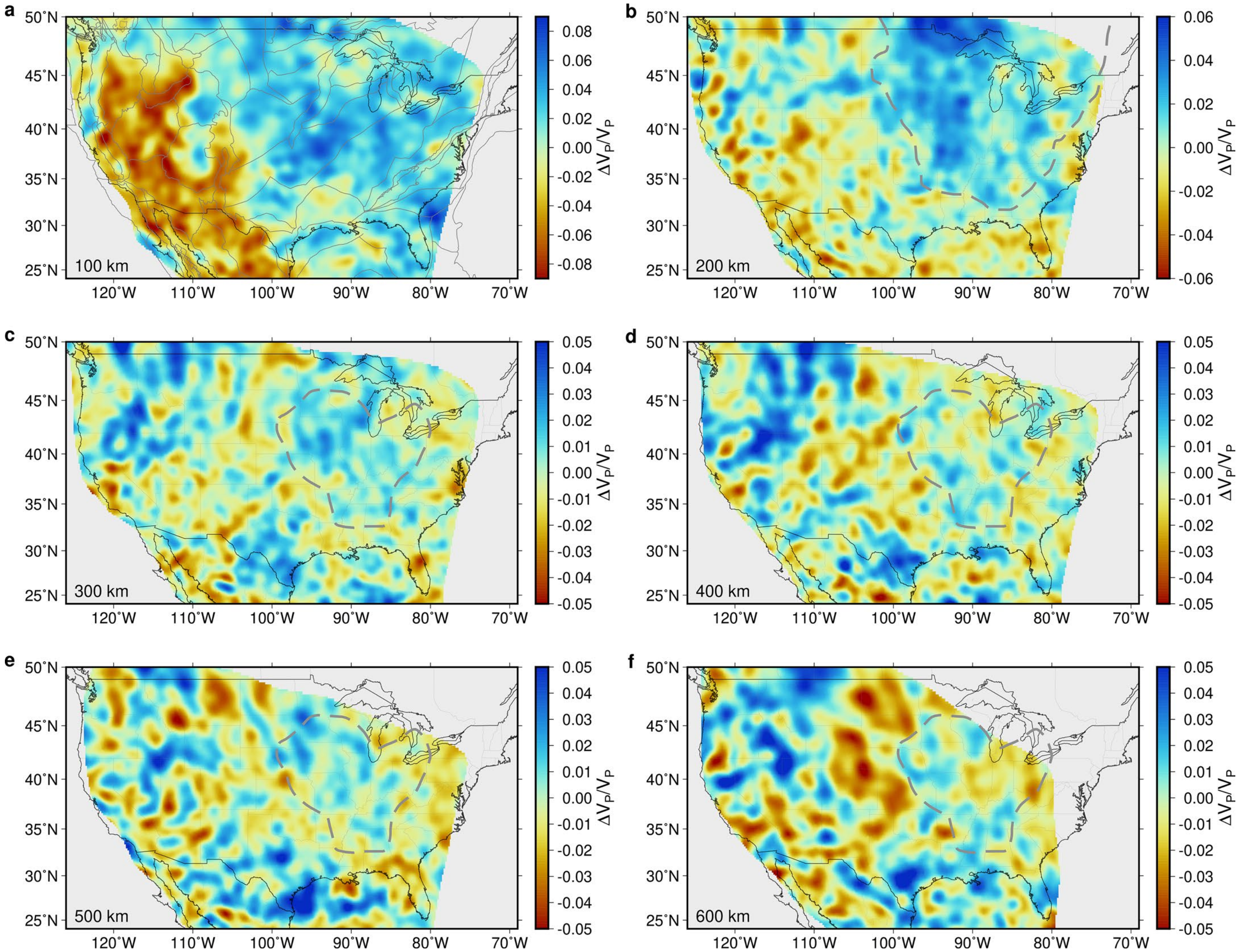

Extended Data Fig. 4 | Isotropic V_P distribution at different depths. a-f. Similar to Extended Data Fig. 3, but are for V_P perturbations at 100, 200, 300, 400, 500, and 600 km depths.

https://doi.org/10.1038/s41561-025-01671-x

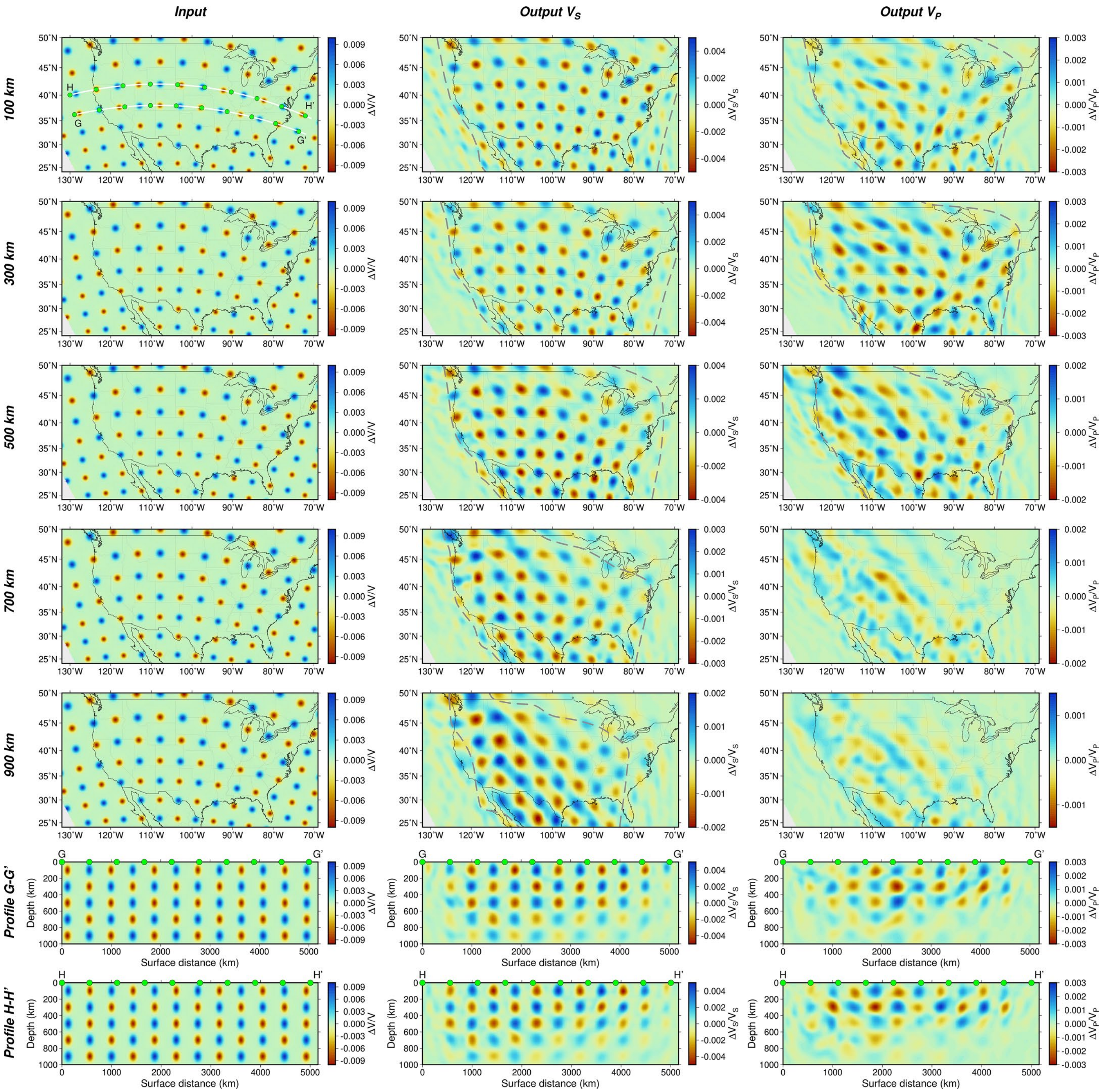

Extended Data Fig. 5 | Resolution tests for SATONA. This multi-panel figure contains 3 columns and 7 rows. The first column shows the input velocity structures, and the second and third columns are outputs for V_S and V_P after 16 iterations of inversions. Though in this figure V_S and V_P are plotted together, and the same input V_S or V_P structure was used, V_S and V_P resolutions are tested separately. The first five rows are velocity maps at 100, 300, 500, 700, and 900 km depths. Regions that are reliable to interpret are outlined by gray dashed lines in the second and third columns for these five rows. The last two rows show two cross-sections that pass through the region with the dripping body (Fig. 2c). Locations of these profiles are shown as white lines on the panel at the first column and first row. Green markers on the cross-sections and the map have the same meaning as in Fig. 2.

https://doi.org/10.1038/s41561-025-01671-x

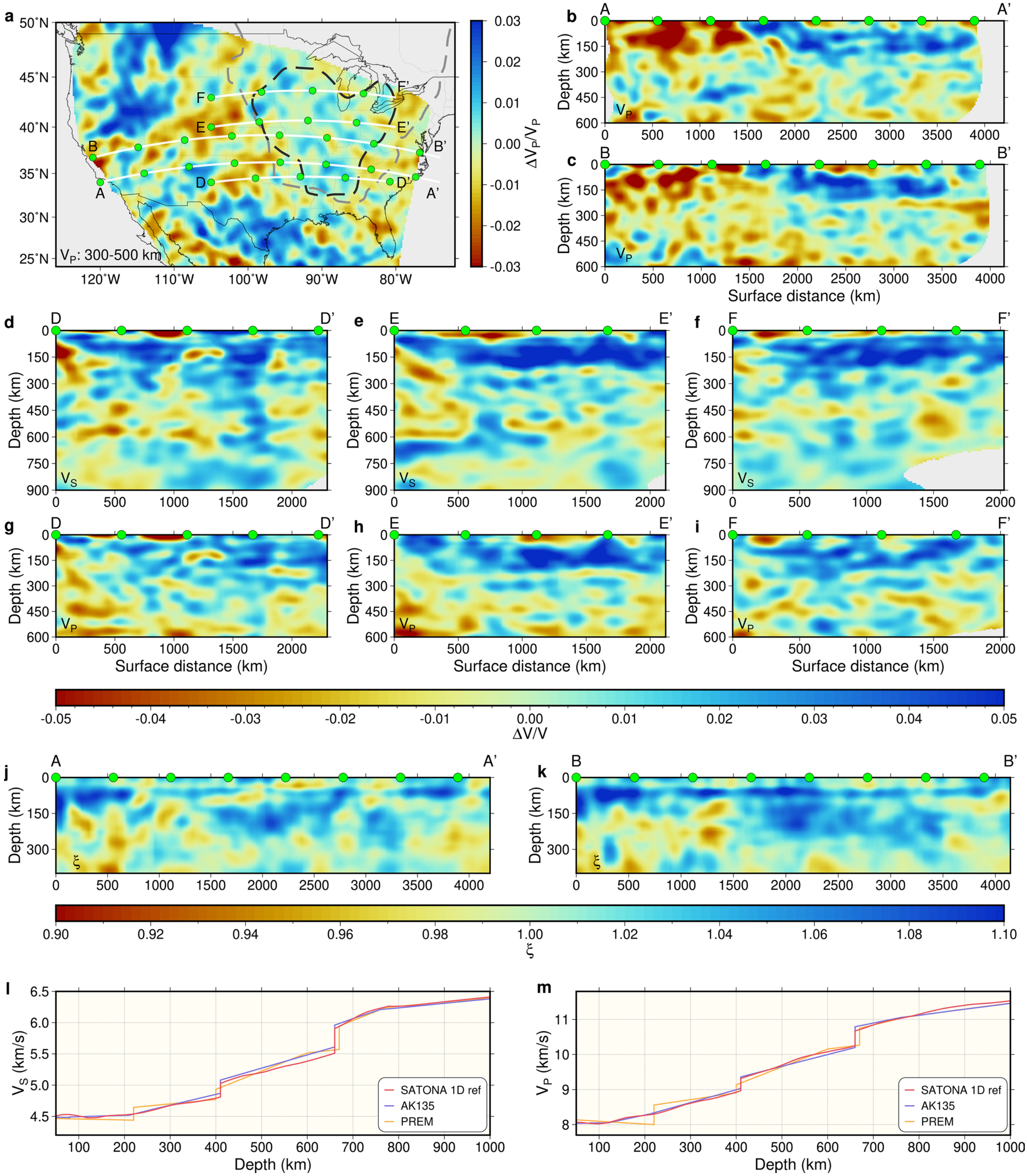

Extended Data Fig. 6 | Velocity perturbation diagrams related to the dripping body, lithospheric anisotropy and the 1D reference velocity model. a. Similar to Fig. 2c, but for V_P. **b-c**. Similar to Fig. 2a,b, but for V_P. **d-f**. Three additional V_S cross-sections that pass through the dripping body at different latitudes. Locations of the profiles are shown as white lines in **a**, and green geographic markers in **a** correspond to ones on top of the cross-sections. **g-i**. Similar to **d-f**, but for V_P. All V_S cross-sections extend to 900 km depths, while V_P ones only extend to 600 km due to the resolution (Extended Data Fig. 5). All cross-sections share a color bar beneath **g-i**. **j-k**. Like Fig. 2a,b, but for the radial anisotropy factor ξ (square of the ratio between SH and SV velocities) in the top 400 km depths. The color bar is beneath the two panels. Horizontally aligned features near Moho might be real or influenced by the assumed Moho depth in CRUST1.0[60]. **l-m**. Mantle 1D reference V_S and V_P structures obtained by averaging the SATONA model (red lines). These models are used to convert absolute velocities to velocity perturbations. AK135[96] (blue lines) and PREM[78] (yellow lines) models are also shown for comparison.

 https://doi.org/10.1038/s41561-025-01671-x

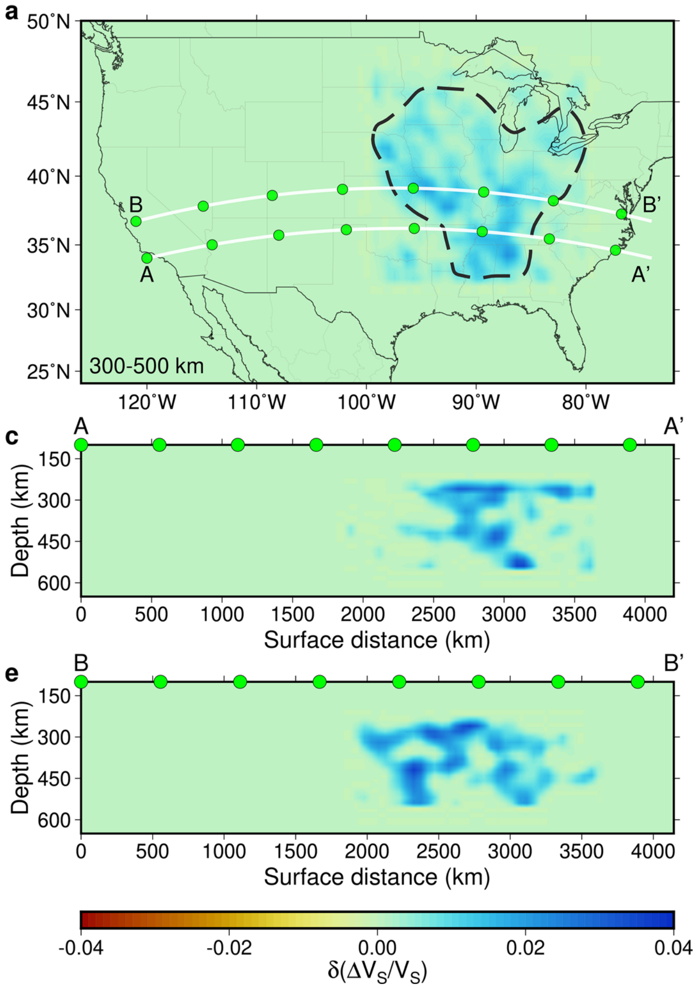

Extended Data Fig. 7 | Resolution test for the dripping body. a–f, Panels in the left column show the dripping structures that are removed for the test. Panels in the right column show the difference in preconditioned $\Delta V_S/V_S$ kernel between original and modified V_S models, and such difference represents the data-favored velocity change to compensate for the removed dripping structures. The three rows correspond to Fig. 2c, a, and b for the average between 300–500 km depths, cross-sections A-A' and B-B'. Locations of the cross-sections are shown in **a**. It is shown that with only one iteration, dripping bodies can be illuminated by the data at the right location.

 https://doi.org/10.1038/s41561-025-01671-x

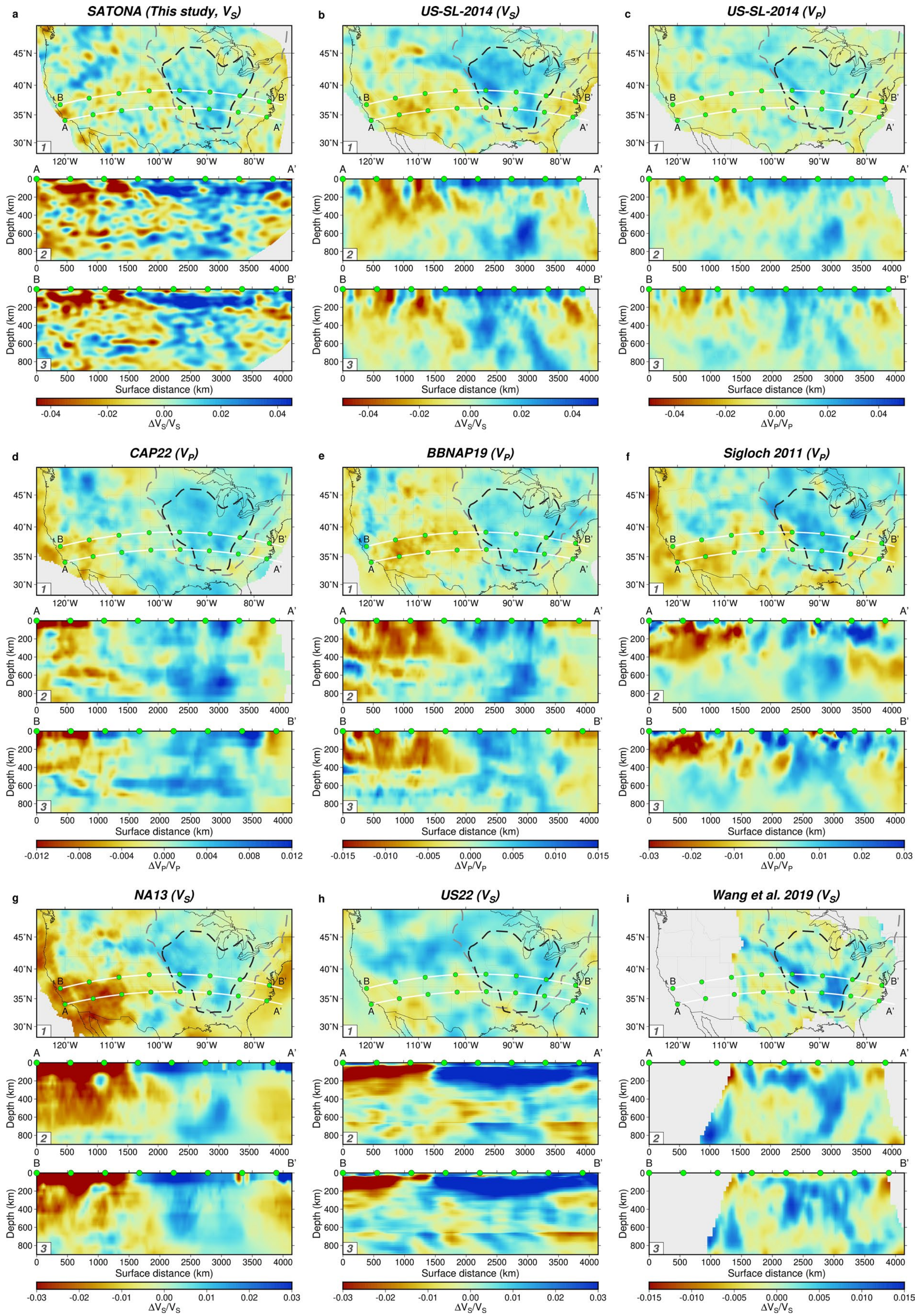

Extended Data Fig. 8 | Comparisons of the dripping structure with previous models. a. V_S from this study. **b.** V_S from US-SL-2014[22]. **c.** V_P from US-SL-2014[22]. **d.** V_P from CAP22[93]. **e.** V_P from BBNAP19[21]. **f.** V_P from ref. 23. **g.** V_S from NA13[94]. **h.** V_S from US22[57]. **i.** V_S from ref. 25. Each panel contains three sub-panels corresponding to Fig. 2c, a and b, for the average between 300 and 500 km depths, cross-sections A-A' and B-B'.

 https://doi.org/10.1038/s41561-025-01671-x

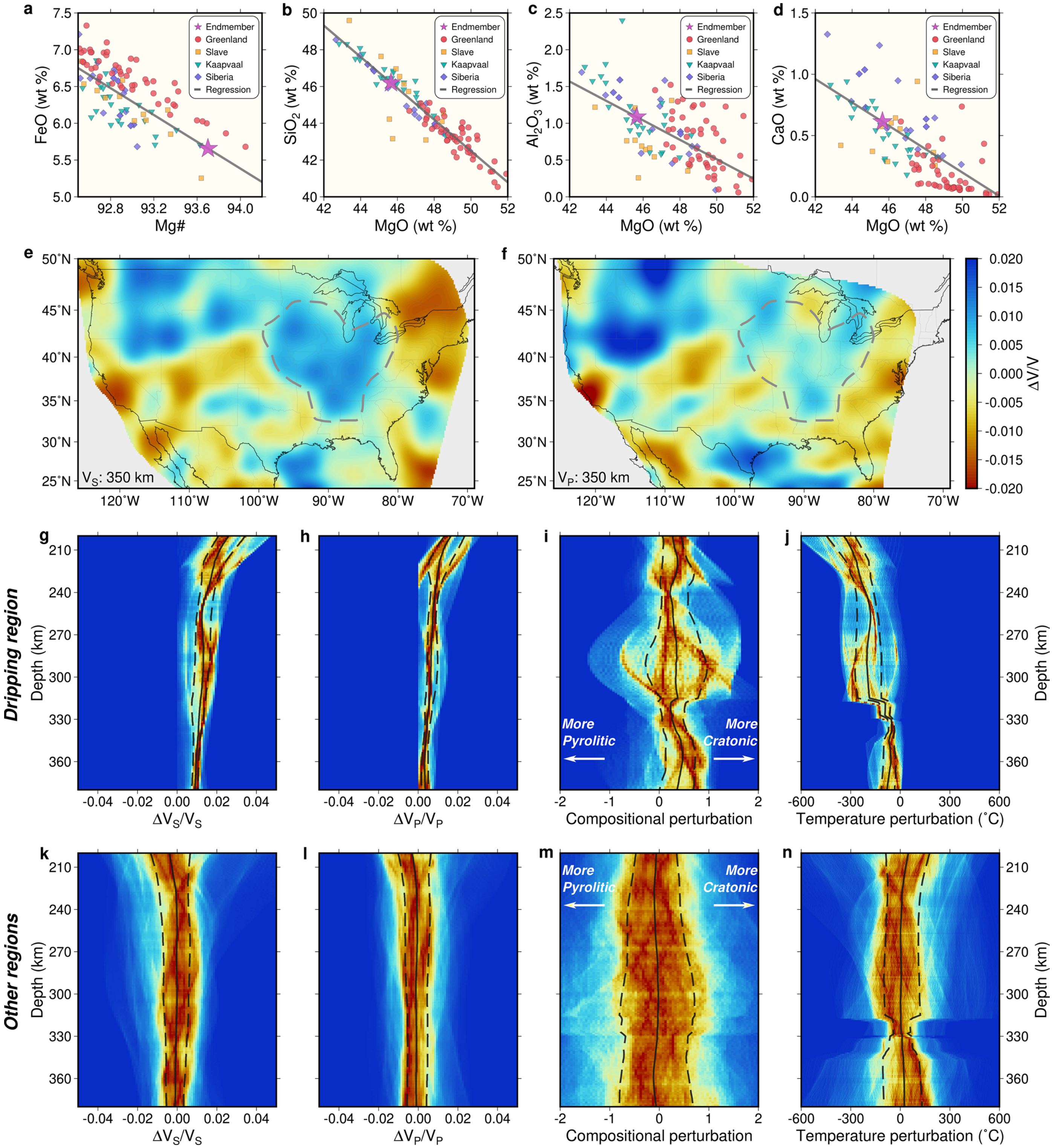

Extended Data Fig. 9 | Thermal and compositional states for the dripping body. a-d. Major element compositions for cratonic lithosphere. The four panels are for Mg#-FeO (**a**), MgO-SiO_2 (**b**), MgO-Al_2O_3 (**c**), and MgO-CaO (**d**) relationships. Samples from different cratons are shown with different symbols, the generalized linear relationships through regression are shown as lines, and the craton endmember used in this study is shown as stars. **e-f**. The smoothed V_S and V_P perturbations at 350 km depth that contribute to Fig. 2d,e. The gray dashed line shows the boundary for dripping bodies, and within it, at each geographic location, the temperature and composition will be estimated later as one sample. **g**. The heatmap of V_S perturbations at different depths for the dripping area (**e**), and warmer colors suggest larger amounts of sample. **h-j**. Similar to **g**, but are for perturbations in V_P (**h**), composition (**i**), and temperature (**j**). A unit in composition represents the compositional difference between the two endmembers as also for Fig. 3d, and higher values are more cratonic. The uncertainty in **i** is big between 250 and 320 km depths, as the difference between V_S and V_P around those depths is not very sensitive to variations in composition. **k-n**. Similar to **g-j**, but for the rest of the regions (regions excluding the dripping area) with good resolution (Extended Data Fig. 5).

https://doi.org/10.1038/s41561-025-01671-x

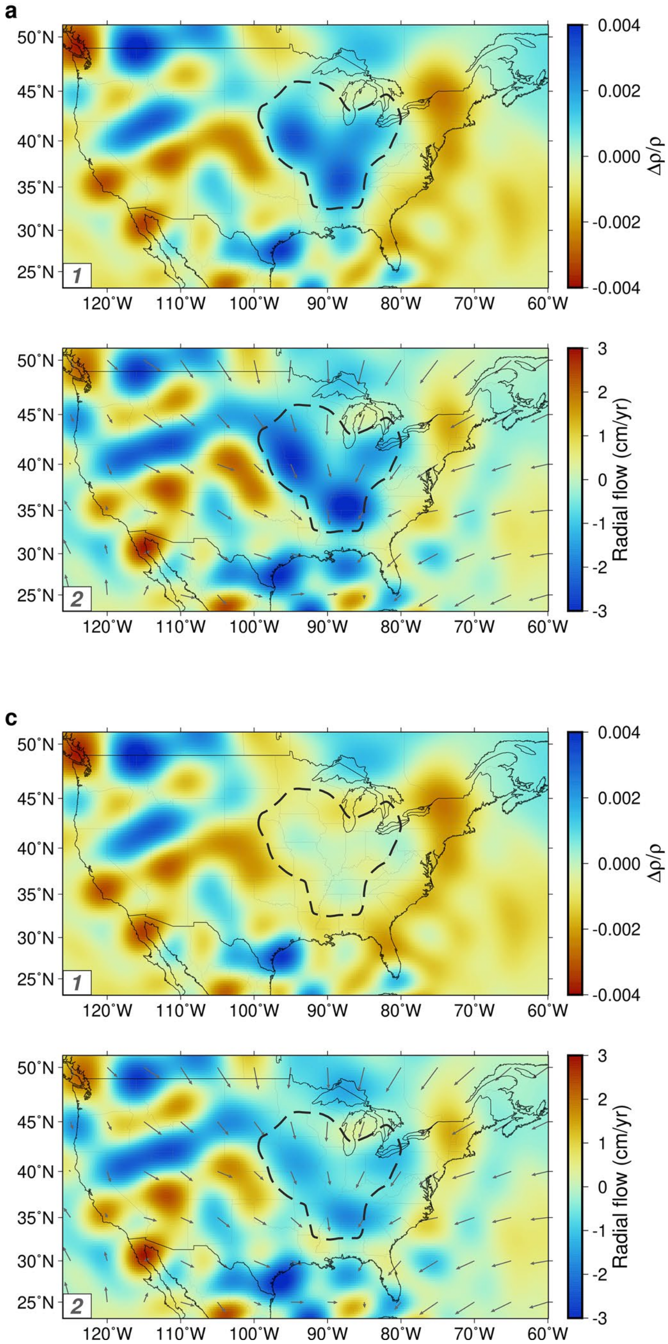

Extended Data Fig. 10 | Upper mantle radial flow for dripping bodies with different densities. Each panel consists of two sub-panels, and the upper sub-panel shows the average density anomaly at 300–500 km depths that drives the mantle flow (spherical harmonic degree < 64), while the lower sub-panel shows the corresponding average radial flow at the same depth range (negative value means flowing downward). Arrows in the lower sub-panels show the average horizontal flow at 300–500 km depths. The four panels are for different V_S-density scaling factors. **a**. Positive V_S perturbations within the dripping area scaled to density the same as the rest of the areas; **b**. V_S perturbations scaled to half of the density perturbations for the rest of the areas; **c**. V_S perturbations scaled to zero; **d**. V_S perturbations scaled to −0.5 of the density perturbations for the rest of the areas so that these dripping bodies are positively buoyant. No matter the assumed density, the dripping area constantly shows downward flows, though weaker when the dripping bodies are more buoyant. Meanwhile, the local density structure has a very limited effect on the horizontal flow, which carries materials from other places to near the dripping area and sink.